NASA/CR—2014-218130

Computational Aerodynamic Simulations of a 1215 ft/sec Tip Speed Transonic Fan System Model for Acoustic Methods Assessment and Development

Daniel L. Tweedt
AP Solutions, Inc., Cleveland, Ohio

October 2014

NASA STI Program . . . in Profile

Since its founding, NASA has been dedicated to the advancement of aeronautics and space science. The NASA Scientific and Technical Information (STI) program plays a key part in helping NASA maintain this important role.

The NASA STI Program operates under the auspices of the Agency Chief Information Officer. It collects, organizes, provides for archiving, and disseminates NASA's STI. The NASA STI program provides access to the NASA Aeronautics and Space Database and its public interface, the NASA Technical Reports Server, thus providing one of the largest collections of aeronautical and space science STI in the world. Results are published in both non-NASA channels and by NASA in the NASA STI Report Series, which includes the following report types:

- TECHNICAL PUBLICATION. Reports of completed research or a major significant phase of research that present the results of NASA programs and include extensive data or theoretical analysis. Includes compilations of significant scientific and technical data and information deemed to be of continuing reference value. NASA counterpart of peer-reviewed formal professional papers but has less stringent limitations on manuscript length and extent of graphic presentations.

- TECHNICAL MEMORANDUM. Scientific and technical findings that are preliminary or of specialized interest, e.g., quick release reports, working papers, and bibliographies that contain minimal annotation. Does not contain extensive analysis.

- CONTRACTOR REPORT. Scientific and technical findings by NASA-sponsored contractors and grantees.

- CONFERENCE PUBLICATION. Collected papers from scientific and technical conferences, symposia, seminars, or other meetings sponsored or cosponsored by NASA.

- SPECIAL PUBLICATION. Scientific, technical, or historical information from NASA programs, projects, and missions, often concerned with subjects having substantial public interest.

- TECHNICAL TRANSLATION. English-language translations of foreign scientific and technical material pertinent to NASA's mission.

Specialized services also include creating custom thesauri, building customized databases, organizing and publishing research results.

For more information about the NASA STI program, see the following:

- Access the NASA STI program home page at *http://www.sti.nasa.gov*

- E-mail your question to *help@sti.nasa.gov*

- Fax your question to the NASA STI Information Desk at 443–757–5803

- Phone the NASA STI Information Desk at 443–757–5802

- Write to:
  STI Information Desk
  NASA Center for AeroSpace Information
  7115 Standard Drive
  Hanover, MD 21076–1320

NASA/CR—2014-218130

Computational Aerodynamic Simulations of a 1215 ft/sec Tip Speed Transonic Fan System Model for Acoustic Methods Assessment and Development

Daniel L. Tweedt
AP Solutions, Inc., Cleveland, Ohio

Prepared under Contract NNC06BA07B, Task NNC07E190T

National Aeronautics and
Space Administration

Glenn Research Center
Cleveland, Ohio 44135

October 2014

Available from

NASA Center for Aerospace Information
7115 Standard Drive
Hanover, MD 21076–1320

National Technical Information Service
5301 Shawnee Road
Alexandria, VA 22312

Available electronically at http://www.sti.nasa.gov

Computational Aerodynamic Simulations of a 1215 ft/sec Tip Speed Transonic Fan System Model for Acoustic Methods Assessment and Development

Daniel L. Tweedt
AP Solutions, Inc.
Cleveland, Ohio 44135

Abstract

Computational Aerodynamic simulations of a 1215 ft/sec tip speed transonic fan system were performed at five different operating points on the fan operating line, in order to provide detailed internal flow field information for use with fan acoustic prediction methods presently being developed, assessed and validated. The fan system is a sub-scale, low-noise research fan/nacelle model that has undergone extensive experimental testing in the 9- by 15-foot Low Speed Wind Tunnel at the NASA Glenn Research Center.

Details of the fan geometry, the computational fluid dynamics methods, the computational grids, and various computational parameters relevant to the numerical simulations are discussed. Flow field results for three of the five operating points simulated are presented in order to provide a representative look at the computed solutions.

Each of the five fan aerodynamic simulations involved the entire fan system, which for this model did not include a split flow path with core and bypass ducts. As a result, it was only necessary to adjust fan rotational speed in order to set the fan operating point, leading to operating points that lie on a fan operating line and making mass flow rate a fully dependent parameter. The resulting mass flow rates are in good agreement with measurement values.

Computed blade row flow fields at all fan operating points are, in general, aerodynamically healthy. Rotor blade and fan exit guide vane flow characteristics are good, including incidence and deviation angles, chordwise static pressure distributions, blade surface boundary layers, secondary flow structures, and blade wakes. Examination of the flow fields at all operating conditions reveals no excessive boundary layer separations or related secondary-flow problems.

Introduction

The development and validation of aircraft engine fan acoustic prediction methods is an important part of ongoing efforts by NASA and industry to reduce noise generation in the fan section of aircraft engines. This work is part of a larger task involving computational fluid dynamics (CFD) to simulate the aerodynamics of selected fan systems, each at several different operating points, for the purpose of providing detailed internal flow field information for use with fan acoustic prediction methods presently being developed, assessed and validated.

This report documents CFD work done on one of the selected fan systems, the Source Diagnostics Test (SDT) fan with rotor R4 and a standard, short-chord stator, both of which were designed by the General Electric Corporation with partial funding from NASA under the Advanced Subsonic Technology program. The SDT fan is a 22-inch sub-scale, low-noise research fan/nacelle model that has undergone extensive experimental testing in the 9- by 15-foot Low Speed Wind Tunnel (LSWT) at the NASA Glenn Research Center [1,2]†.

† Numbers in square brackets indicate references.

Fan Geometry

A meridional plane drawing of the SDT fan system is shown in Figure 1, with all major components depicted and shown to scale. The fan rotor blade stacking line is the zero-reference axial location, and the fan exit guide vane (FEGV) row is a short-chord, high vane-count, standard design with the trailing-edge stacking line located 8.807 inches axially downstream of the rotor blade stacking line. The number of blades for each blade row is indicated in parenthesis. The rotating portion of the rotor hub includes the entire upstream centerbody/spinner, and extends about 0.150 inches downstream of the rotor to axial location 1.640 inches (see Figure 1, mark below hub contour near rotor trailing edge).

Five aerodynamic simulation cases were defined for the SDT fan, each at a different rotational speed on the fan operating line. In all cases mechanical speed is equal to corrected speed since the far-field flow is at standard day sea-level total (stagnation) conditions. Rotor blade coordinates were provided for the running (hot) blade shape at three of the five fan operating points: sea-level takeoff (SLTO), cutback, and approach, corresponding to corrected rotational speeds of 12657, 11075, and 7809 rpm, respectively. Blade coordinates for the other two rotational speeds, 11771 and 9493 rpm, were determined by linear interpolation. The corrected rotor blade tip speed for the SLTO operating point is 1215 ft/sec. Running rotor tip clearances were measured at blade leading edge, mid-chord, and trailing edge locations, over the entire range of rotational speeds, and quadratic regression curve fits of the measured data were used to determine the clearances at each of the selected rotational speeds. Table 1 summarizes these results. Quadratic functions defined from the data in Table 1 were used for calculating the chordwise distributions of tip clearance, which are shown in Figure 2.

Table 1: Rotor Blade Tip Clearances

Operating Point	Rotational Speed (rpm)	Leading Edge Tip Clearance (mils)	Mid-Chord Tip Clearance (mils)	Trailing Edge Tip Clearance (mils)
SLTO	12,657	34.87	31.86	39.74
	11,771	36.40	34.08	41.82
Cutback	11,075	37.57	35.75	43.42
	9,493	40.09	39.35	46.96
Approach	7,809	42.58	42.86	50.60

Computational Fluid Dynamics

Two different CFD codes were used to simulate the airflow around and through the fan system: an axisymmetric viscous solver called AVCS, and a three-dimensional viscous turbomachinery solver called TSWIFT. Multiple solution domains (grid blocks) were used, with axisymmetric solutions coupled to three-dimensional solutions at mixing planes by means of a separate computer program called SMPI, developed as a companion program for AVCS and

TSWIFT. SMPI was also used to couple rotating and stationary three-dimensional solutions together at mixing planes. In general, the three-dimensional TWSIFT solver was used for computational domains in and near blade rows, and the axisymmetric AVCS solver was used for computational domains sufficiently far away from blade rows†.

The AVCS and TSWIFT codes use similar numerical algorithms; both solve the Reynolds-averaged Navier-Stokes equations on body-fitted grids using an explicit, finite-difference scheme. The codes include viscous terms in the body-normal direction(s), but neglect them in the streamwise direction by applying the thin-layer approximation. The discretized equations are solved with a multi-stage Runge-Kutta time-marching scheme using a spatially varying time step, implicit residual smoothing, and preconditioning [3-6]. All simulations described herein were run using a 2-stage Runge-Kutta scheme with a CFL number of 2.5, and using the AUSM+ upwind scheme [7] for best accuracy.

The TSWIFT code was derived from, and has the same basic features as the SWIFT code [8] developed by Chima at the NASA Glenn Research Center. TSWIFT also has a fairly general multiblock capability (when used with SYNCEX; see preceding footnote), includes the two-equation SST turbulence model developed by Menter [9], and implements Giles' two-dimensional, steady-state, non-reflecting boundary conditions [10,11] at flow inlet, exit, and mixing-plane boundaries‡. Note that when a two-equation turbulence model is used, either the Wilcox k-ω model [12] or the Menter SST model, it is necessary to pitchwise average the computed turbulence properties on the upstream side of the mixing plane. In that case the turbulence kinetic energy, k, and the ratio of turbulence kinetic energy to turbulence dissipation rate, k/ω, are each mass-averaged, and the resulting average values of k and (indirectly) ω are used as inflow boundary values for the domain on the downstream side of the mixing plane.

Computational Grids

An axisymmetric grid consisting of four two-dimensional grid blocks, shown in Figure 3, was used outside of the fan system blade rows. For clarity, only some of the grid lines are drawn, and the different blocks are shown in various colors: a far-field block (green), an external nacelle block (blue), an upstream/inlet block (black), and a nozzle/downstream block (black). The far-field block size is 177×45 nodes, the external nacelle block size is 321×65 nodes, and the upstream/inlet and nozzle/downstream block sizes are each 169×85 nodes. The far-field block overlaps the top of the nacelle block, but the grid nodes are not aligned, so the computational solutions are interpolated there. The bottom of the nacelle block does not overlap the upstream/inlet and nozzle/downstream blocks, but the boundary-normal grid spacings are relatively small and the boundary nodes are aligned.

The nacelle, inlet, and nozzle grid blocks were all generated using a Poisson partial differential equation (PDE) solver, otherwise known as an elliptic grid generator, which produces grids with good boundary-normal node clustering and spacings, and generally good local orthogonality. Since the CFD method always directly includes the viscous sublayer in the near-

† All program-to-program communications, for mixing planes and direct block-to-block interfaces, were handled using a facility called SYNCEX (pronounced “sink-ex”). SYNCEX is a message-passing interface that enables two or more executing programs to efficiently exchange data on a single computer and/or over a network.

‡ The SMPI code also implements Giles' two-dimensional, steady-state, non-reflecting boundary conditions.

wall treatment of turbulent boundary layers – wall functions are not used – the node spacings at solid walls are small. In the inlet and on the external surface of the nacelle the wall-normal spacing is nominally 0.0001 inches, whereas in the nozzle the wall-normal spacing is nominally 0.0003 inches. Corresponding inner-variable wall distances, y^+, are generally between 1.0 and 3.0.

An enlarged view of the two-dimensional grid in and around the fan system is shown in Figure 4, where every other grid line is drawn. In this figure the elliptic grid stretching for the nacelle, inlet, and nozzle grid blocks can be seen more easily. Magnified views of the grid around the nacelle leading edge and trailing edge are shown in Figure 5.

Meridional locations of the three-dimensional blade row grid blocks are shown in Figure 6, with flow boundaries indicated by dashed and dash-dotted lines. The blue dash-dotted lines indicate grid block direct-interfaces, and the black dashed lines indicate mixing-plane interfaces. There are three primary grid blocks for the rotor: the rotor inlet H-grid block, the rotor blade row C-grid block, and the rotor exit H-grid block. The FEGV computational domain involves a single C-grid block. The red streamlines in Figure 6 show stream-surface locations for blade-to-blade (streamwise-pitchwise) grid views, as well as for blade-to-blade flow contour plots, to be shown later.

The blade row grids, except for the rotor exit H-grid block, were generated using a computer program called TTGRID, which is a modified version of TCGRID [13], a grid generator for turbomachinery developed by Chima at the NASA Glenn Research Center. TTGRID applies an elliptic PDE solver to the blade-to-blade mesh surfaces of blade row C- and H-grids.

Meridional plane projections of the three-dimensional blade row grid blocks at grid surfaces located about mid-pitch between the blades are shown in Figures 7. Rotor grid blocks are drawn in black and green, and the FEGV grid is drawn in red. For clarity, only every other grid line in the streamwise direction is shown, although all grid lines in the spanwise direction are drawn. Corresponding three-dimensional views of the grid blocks are provided in Figures 8 and 9, again with only some of the grid lines drawn. The rotor C-grid (black) has a size of 217×49×85 nodes, the rotor inlet H-grid (green) has a size of 33×42×85 nodes, and the rotor exit H-grid (green) has a size of 153×89×81 nodes. Note that the rotor inlet H-grid overlaps the rotor blade C-grid and has node-to-node alignment with it. The rotor exit H-grid also overlaps the rotor blade C-grid, but the grid nodes are not aligned. The FEGV C-grid (red) has a size of 209×45×73 nodes. All of the three-dimensional grids have boundary-normal node spacings which are nominally 0.0002 inches at blade/vane surfaces, and 0.0003 inches at endwall surfaces.

Streamwise-pitchwise views of the rotor grid at three spanwise locations, corresponding to the red streamlines in Figure 6, are shown in Figure 10, with every other grid line drawn (every fourth line in the streamwise direction for the exit H-grid block). Corresponding pitchwise-spanwise views of the rotor C-grid and exit H-grid at the respective block downstream boundaries are shown in Figure 11.

Over the rotor blade tip, in the endwall clearance gap, an O-grid block of size 179×13×17 nodes is used. The tip clearance grid is shown in Figure 12, which includes magnified views around the blade leading- and trailing-edges, and a magnified axial cross-section view near mid-chord. All grid lines are drawn for the magnified views. Note that the tip clearance grid overlaps the rotor blade C-grid and has node-to-node alignment with it.

A streamwise-pitchwise view of the FEGV grid near midspan, corresponding to the middle red streamline in Figure 6, is shown in Figure 13. Shown below the full view are magnified views of the vane leading and trailing edge regions. For clarity, only every other grid line parallel to the vane surface is drawn for the full view. A corresponding pitchwise-spanwise view of the FEGV grid at the block downstream boundary is shown in Figure 14.

All of all computational grid blocks and their respective sizes are summarized below in Tables 2 and 3.

Table 2: Two-Dimensional Grid Blocks

Grid Block	Size (I×J×K)	Number of Nodes
Fan System Upstream/Inlet	169×85	14,365
Fan System Nozzle/Downstream	169×85	14,365
Fan System External Nacelle	321×65	20,865
Fan System Far Field	177×45	7,965
Total All Blocks		57,560

Table 3: Three-Dimensional Grid Blocks

Grid Block	Size (I×J×K)	Number of Nodes
Rotor Inlet H-Grid	33×42×85	117,810
Rotor Blade C-Grid	217×49×85	903,805
Rotor Exit H-Grid	153×89×81	1,102,977
Rotor Tip Clearance O-Grid	179×13×17	39,559
FEGV C-Grid	209×45×73	686,565
Total All Blocks		2,850,716

To conclude this section, the rotor exit H-grid block and its relative importance to the CFD solutions will be discussed. It is perhaps apparent that this grid block involves a relatively large number of grid nodes, even though it contains no blade surfaces and is essentially just a downstream extension of the rotor blade C-grid. The higher grid density is necessary, however, to provide the numerical resolution needed for accurate wake convection, and to achieve a reasonable level of grid independence for the CFD solution. If the grid is too coarse, particularly in regions where the flow field involves large gradients and the primary flow is not aligned with the grid, then numerical dissipation is excessive and causes substantial distortion of computed local flow features. More specifically, excess artificial dissipation causes the computed wake and blade tip vortex to decay too rapidly.

If the primary purpose of the CFD simulations were only aerodynamic performance assessment and/or prediction, then the lack of local flow field accuracy in the wake region might not be crucial because local accuracy typically has a relatively small influence on spatially averaged performance quantities. For the current task, however, the computed rotor wake and tip-vortex structures are important because they define flow field characteristics associated with noise generation. Particularly important are the computed flow field results at the rotor exit H-grid downstream boundary (and mixing plane) since these are intended for direct use in acoustic methods assessment, research and development.

Fan System Aerodynamic Simulations

All CFD simulations were run with the far-field (free stream, flight) Mach number set at 0.100, with total (stagnation) conditions set at standard day sea-level values. The corresponding unit Reynolds number is 5.915E+05 inches^{-1}. Air is modeled as a perfect gas with a ratio of specific heats, γ, equal to 1.400.

The effects of turbulence were modeled using the two-equation SST turbulence model [9], with free stream turbulence on the far-field upstream boundary set at 0.2 percent, along with a turbulence (eddy) viscosity equal to 0.2 times the molecular viscosity, giving a turbulence length scale of 1.39E-03 inches. The corresponding turbulence kinetic energy is 5.99E-08 (dimensionless; multiply by square of free stream stagnation speed-of-sound to obtain a dimensional value)[†]. In all the cases simulated, rotor blade laminar-to-turbulent boundary layer transition occurred near the leading edge, at a location around 5 percent of blade chord.

Measured and computed values of the fan mass flow rate are listed below in Table 4. All five of the CFD simulation cases were run until the maximum and average (RMS) solution residuals were reduced by 4 to 5 orders of magnitude. Similar levels of convergence were obtained for performance-related quantities such as mass flow rate, average total temperature, and average total pressure. Integrated mass flow conservation discrepancies for the computed solutions are small, being everywhere less than ±0.06 percent.

† At the fan inlet the turbulence is lower than originally intended because of turbulence decay upstream of the inlet, and because of an error in calculating the inlet boundary values so as to account for that decay. The turbulence is not so low, however, that it significantly affects the computed aerodynamics. Turbulence at the fan inlet is nominally about 0.03 percent, with a turbulence viscosity of 0.2 times the molecular viscosity and a turbulence kinetic energy of around 3.5E-08.

Table 4: Measured and Computed Fan Flow Rates

Operating Point	Rotational Speed (rpm)	Measured Flow Rate (lbm/sec)	Computed Flow Rate (lbm/sec)	Flow Rate Difference (percent)
SLTO	12,657	97.34	97.23	-0.11
	11,771	89.66	89.53	-0.14
Cutback	11,075	83.89	83.48	-0.49
	9,493	70.83	70.52	-0.44
Approach	7,809	57.86	57.97	0.19

The measured and computed mass flow rates in Table 4 differ by -0.49 to 0.19 percent, depending on operating point. The uncertainty in measured flow rate is estimated to be at least ±0.5 percent, so there is some uncertainty regarding exactly how much the computed and measured flow rates differ. In any case, the differences are not large enough to substantially compromise the intended use of the computational results; that is, for acoustic methods assessment, research and development.

Selected results from three of the five CFD simulation cases are presented below. Flow field contour plots are presented for results at the SLTO, cutback, and approach operating points, the primary purpose being to provide a representative look at the computed solutions. More extensive and detailed flow field information can be obtained directly from the CFD grid and solution data sets, which are being made available along with this report, or which can be obtained separately upon request.

Mach number contours for the entire fan system flow field at the SLTO operating point are shown in Figure 15, where the three-dimensional blade-row solutions have been mixed-out averaged in the pitchwise direction. An enlarged view of the fan region is shown in Figure 16, and a corresponding contour plot of turbulence kinetic energy, mass-averaged in the pitchwise direction, is shown in Figure 17.

Rotor blade-to-blade relative (rotating system) Mach number contours for the SLTO operating point are shown in Figures 18a and 18b. Figure 18a shows a near tip section at about 89 percent span from the hub, and Figure 18b shows near midspan and near hub sections at about 51 and 11 percent span, respectively (see red streamlines in Figure 6). Relative Mach number contours in and around the rotor tip endwall clearance gap are shown in Figure 19, where the tip mid-clearance-gap location is roughly 0.020 inches from the casing endwall, and the mid-chord axial location is at the rotor blade stacking line. Corresponding contours of relative Mach number at the rotor C-grid downstream boundary, located 0.550 inches downstream of the rotor trailing edge, are shown in Figure 20, and contours of various flow properties at the rotor exit H-grid downstream boundary, which is the downstream mixing plane, are shown in Figures 21a and 21b. Figure 21a shows relative and absolute (stationary system) Mach number contours, and Figure 21b shows entropy and turbulence kinetic energy contours. Note that the entropy is non-dimensionalized by the gas constant, R, and is zero at the upstream reference condition.

FEGV blade-to-blade absolute Mach number contours for fan operation at the SLTO operating point are shown in Figures 22a and 22b. Figure 22a shows a vane section at about 89 percent span from the hub, and Figure 22b shows vane sections at about 51 and 11 percent span (see red streamlines in Figure 6). Corresponding Mach number contours at the FEGV downstream mixing plane are shown in Figure 23.

Mach number contours for the entire fan system at the cutback operating point are shown in Figure 24, with an enlarged view of the fan region shown in Figure 25. Again, the three-dimensional blade-row solutions have been mixed-out averaged in the pitchwise direction. Corresponding rotor blade-to-blade relative Mach number contours are shown in Figures 26a and 26b, and various flow property contours at the rotor downstream mixing plane are shown in Figures 27a and 27b. Flow field contours for the FEGV at cutback operation are not shown, but are aerodynamically similar to those at SLTO.

Mach number contours for the entire fan system at the approach operating point are shown in Figure 28, with Figure 29 showing an enlarged view of the fan region. Corresponding rotor blade-to-blade relative Mach number contours are shown in Figures 30a and 30b, and various flow property contours at the rotor downstream mixing plane are shown in Figures 31a and 31b. Absolute Mach number contours for the FEGV are shown in Figures 32a and 32b, and in Figure 33. The computed FEGV flow field, like that for cutback operation, is aerodynamically similar to the SLTO solution, although it might be noted that the FEGV suction-surface/hub corner flow separation is significantly weaker for the approach operating point (compare Figure 32b to Figure 22b, and Figure 33 to Figure 23). In general, however, despite some non-conformity, the similar solutions show that the FEGV flow field scales more-or-less with flow rate for all simulated operating points on the fan operating line.

Concluding Remarks

The entire fan system was aerodynamically simulated for five operating points, requiring only fan rotational speed to be adjusted as the independent parameter when setting each operating point. As a result, the computed operating points lie on a fan operating line, and mass flow rate is a dependent parameter. Computed and measured fan system mass flow rates are in good agreement, indicating indirectly that the computational and experimental fan operating lines are nearly the same.

The computed blade row flow fields at all operating points are, in general and as expected, aerodynamically healthy. Rotor blade and FEGV flow characteristics are good, including incidence and deviation angles, chordwise static pressure distributions (not shown, but can be inferred from Mach number distributions), blade surface boundary layers, secondary flow structures, and blade wakes. Examination of the computed flow fields reveals no excessive or critical boundary layer separations or related secondary flow problems.

References

1. Podboy, Gary G., Krupar, Martin J., Hughes, Christopher E., Woodward, Richard P., “Fan Noise Source Diagnostic Test— LDV Measured Flow Field Results,” NASA TM-2003-212330 (also AIAA-2002-2431), July 2003.
2. Hughes, Christopher E., Jeracki, Robert J., Woodward, Richard P., “Fan Noise Source Diagnostic Test— Rotor Alone Aerodynamic Performance Results,” NASA TM-2005-211681 (also AIAA-2002-2426), April 2005.
3. Chima, R. V., "Viscous Three-Dimensional Calculations of Transonic Fan Performance," in CFD Techniques for Propulsion Applications, AGARD Conference Proceedings No. CP-510, AGARD, Neuilly-Sur-Seine, France, February 1992, pp 21-1 to 21-19 (also NASA TM-103800).
4. Chima, R. V., and Yokota, J. W., "Numerical Analysis of Three-Dimensional Viscous Flows in Turbomachinery," AIAA Journal, Vol. 28, No. 5, May 1990, pp. 798-806.
5. Tweedt, Daniel L., and Chima, Rodrick V., "Rapid Numerical Simulation of Viscous Axisymmetric Flow Fields," NASA TM-107103 (also AIAA-96-0449), November 1995.
6. Tweedt, Daniel L., Chima, Rodrick V., and Turkel, Eli, "Preconditioning for Numerical Simulation of Low Mach Number Three-Dimensional Viscous Turbomachinery Flows," NASA TM-113120 (also ICOMP-97-11 and AIAA-97-1828), October 1997.
7. Chima, R. V. and Liou, M.-S., “Comparison of the AUSM+ and H-CUSP Schemes for Turbomachinery Applications,” AIAA Paper AIAA-2003-4120 (also NASA TM-2003-212457).
8. Chima, R. V., “Swift – Multiblock Analysis Code for Turbomachinery,” User's Manual and Documentation, Version 300, August 2003.
9. Menter, R. F., “Two-Equation Eddy-Viscosity Turbulence Models for Engineering Applications,” AIAA Journal, Vol. 32, No. 8, August 1994, pp. 1598-1605 (also NASA TM-111958).
10. Giles, Michael B., “Nonreflecting Boundary Conditions for Euler Equation Calculations,” AIAA Journal, Vol. 28, No. 12, December 1990, pp. 2050-2058.
11. Giles, Michael, “UNSFLO: A Numerical Method For The Calculation Of Unsteady Flow In Turbomachinery,” GTL Report No. 205, May 1991, pp. 45-56.
12. Wilcox, David C., *Turbulence Modeling for CFD*, DCW Industries, Inc., La Cañada, CA, Third edition, 2006.
13. Chima, R. V., “TCGRID 3-D Grid Generator for Turbomachinery, User's Manual and Documentation,” Version 300, July, 2003.

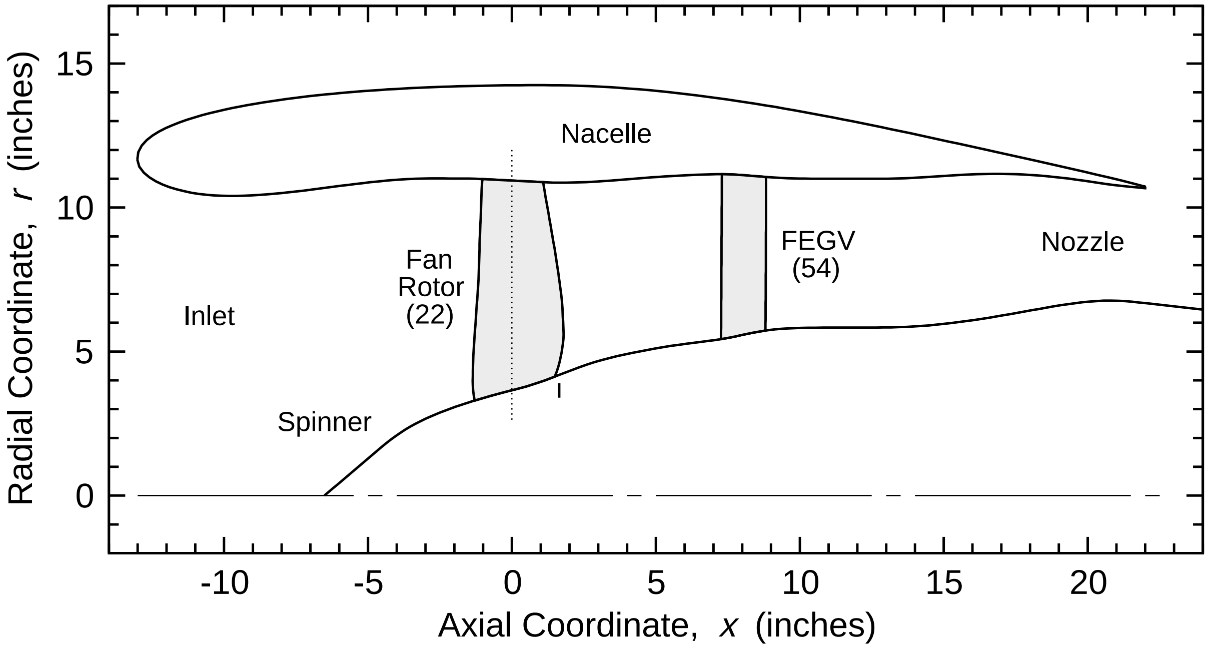

Figure 1: Schematic Drawing of the SDT Fan System

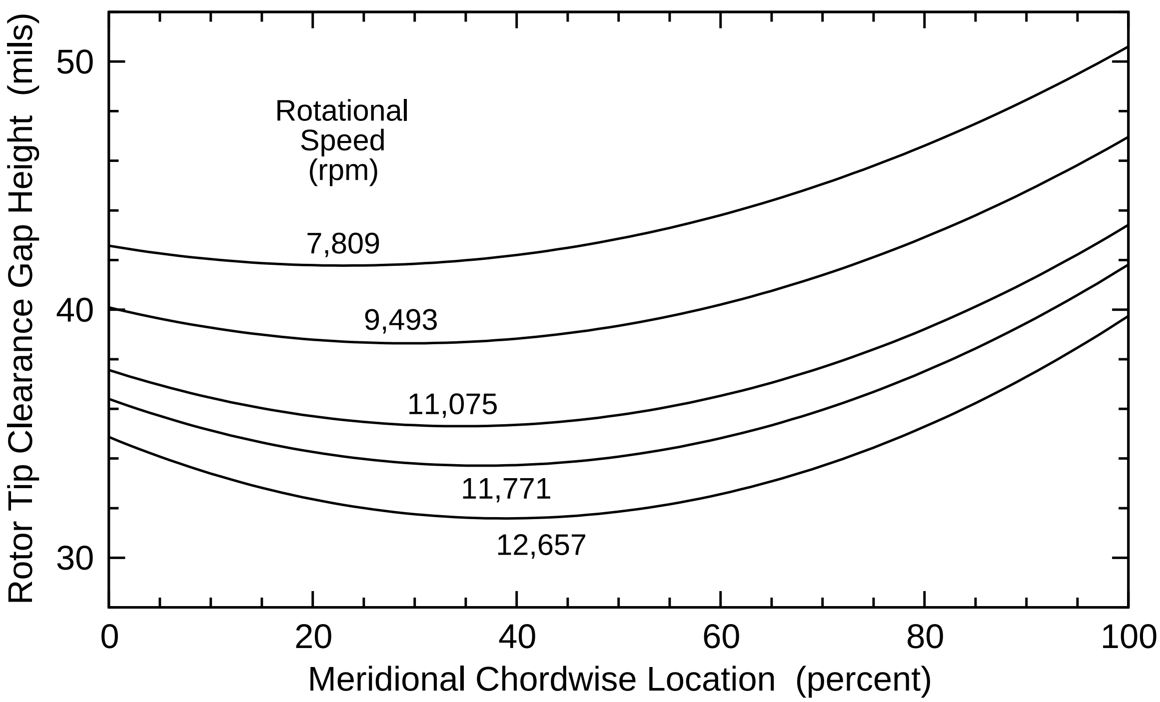

Figure 2: Chordwise Distributions of Rotor Blade Tip Clearance

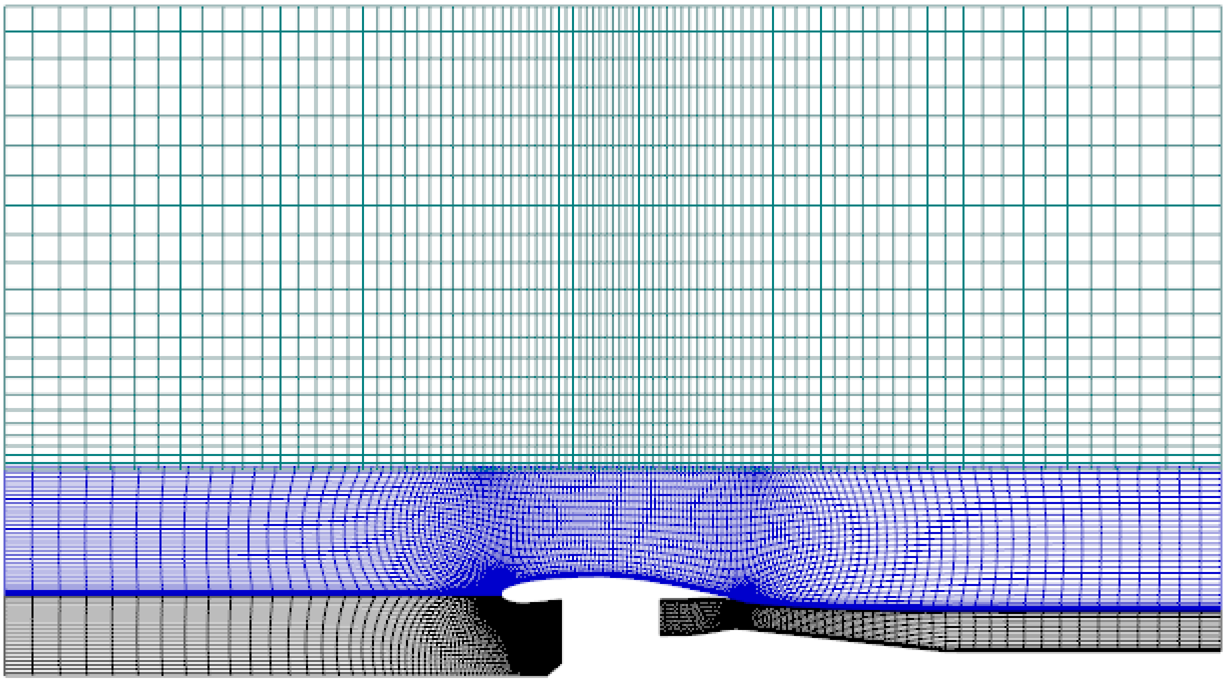

Figure 3: Two-Dimensional Axisymmetric CFD Grid Blocks (Entire Computational Domain)

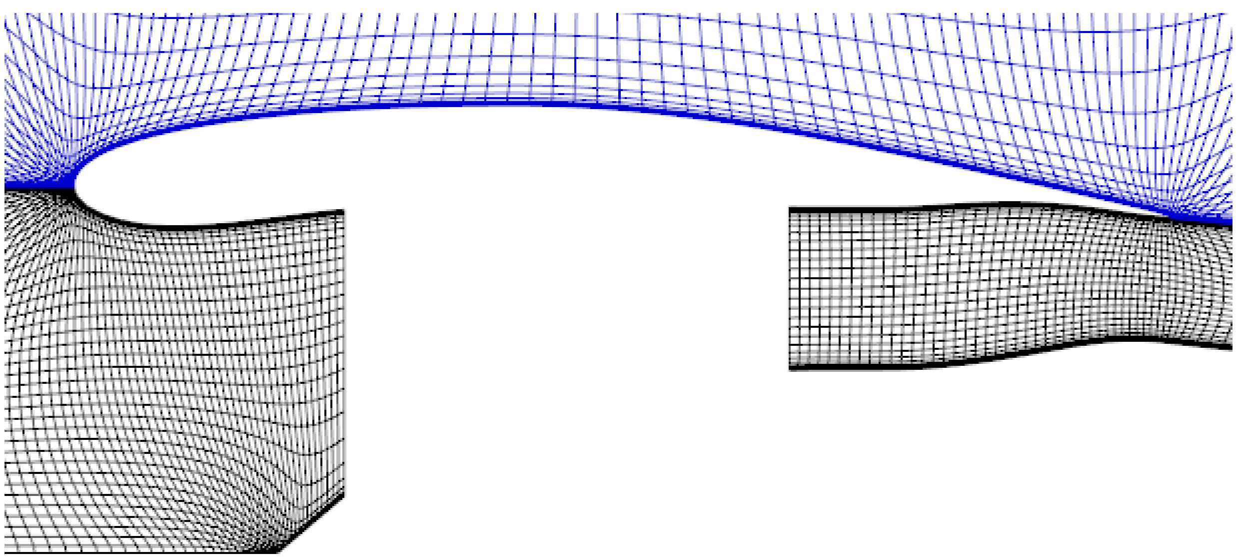

Figure 4: Enlarged Inlet, Nozzle, and Nacelle Grid Blocks

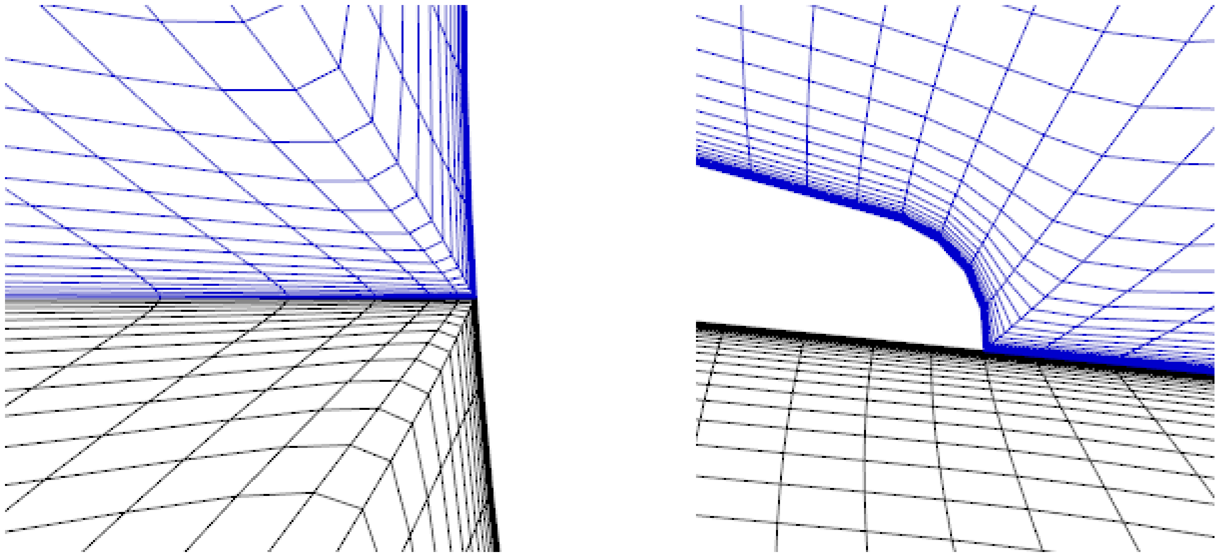

Figure 5: Magnified Nacelle Leading and Trailing Edge Grids

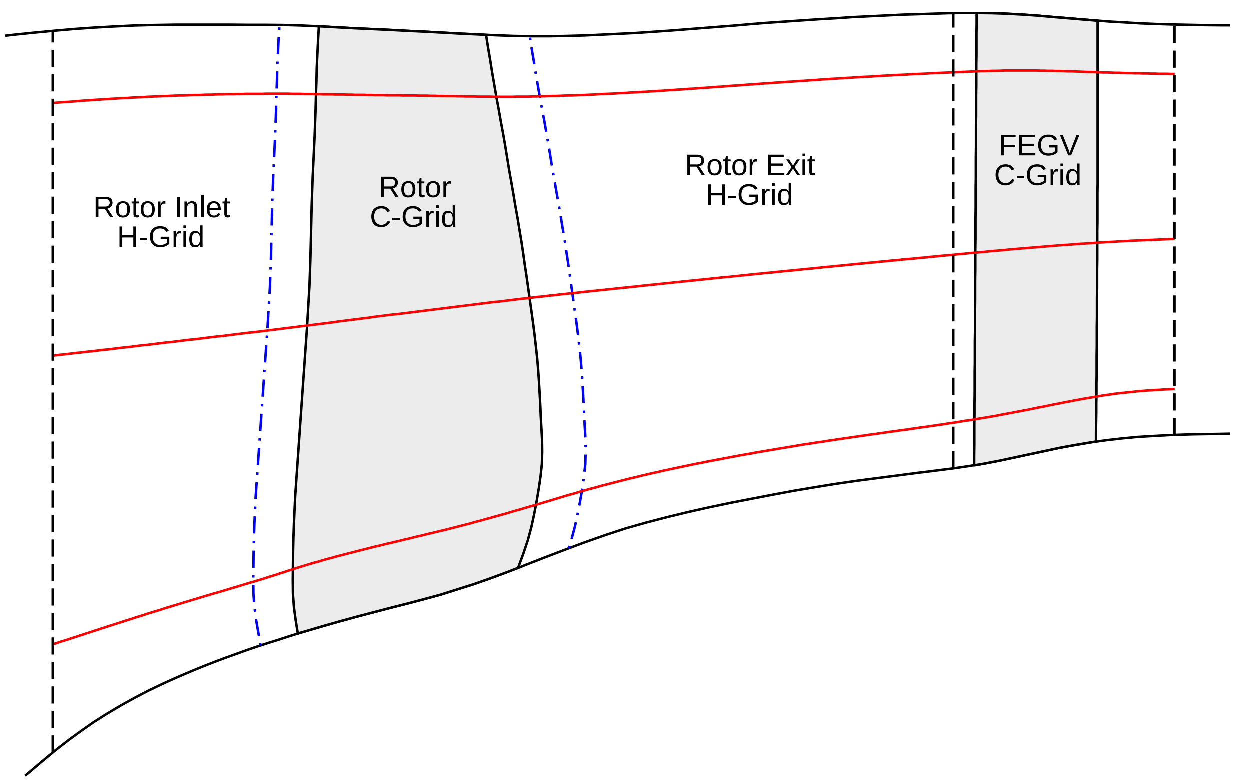

Figure 6: Meridional Location and Extent of Three-Dimensional CFD Grid Blocks

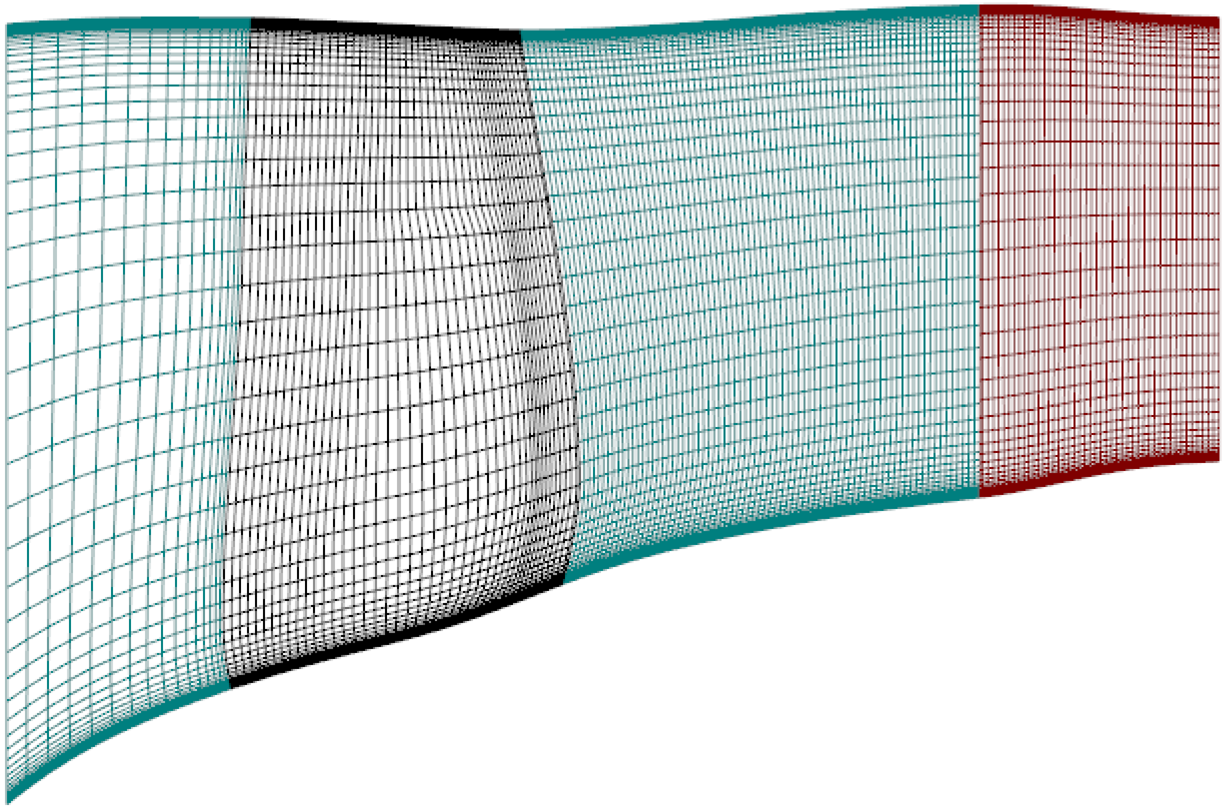

Figure 7: Meridional View of Three-Dimensional CFD Grid Blocks (Mid-Pitch Location)

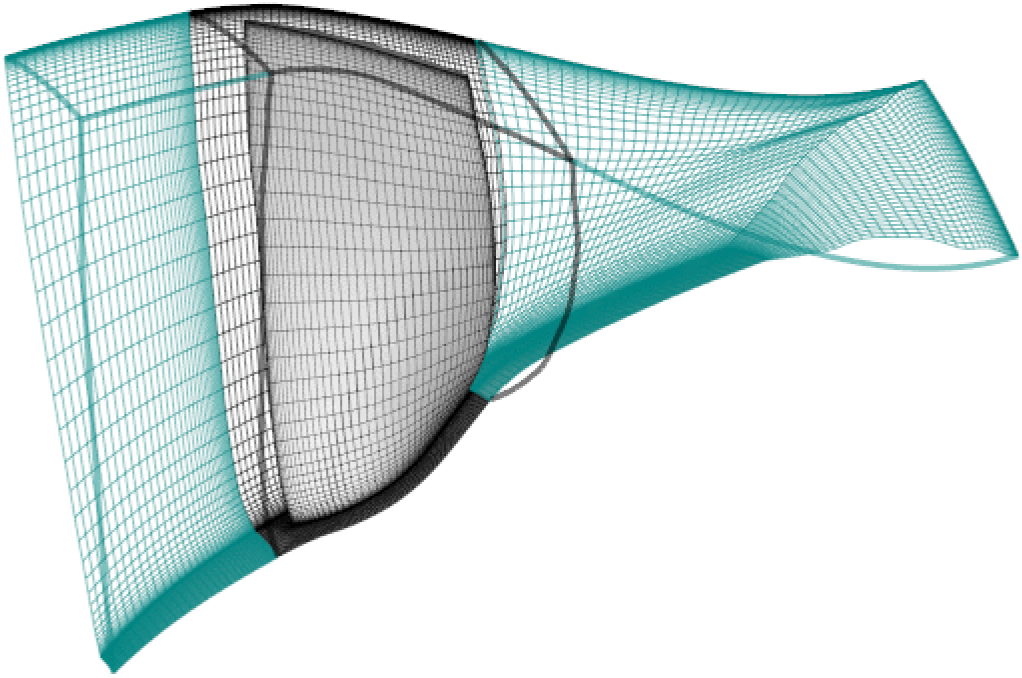

Figure 8: Three-Dimensional View of Rotor Grid

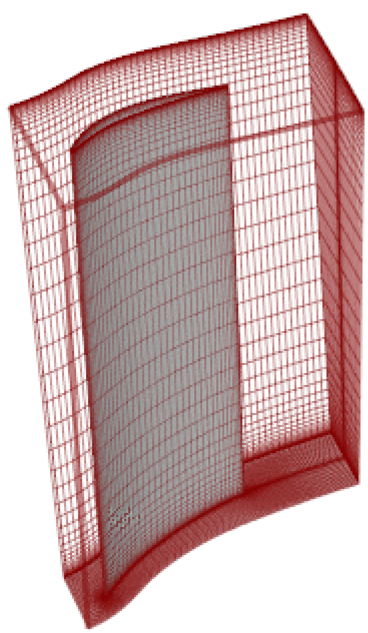

Figure 9: Three-Dimensional View of FEGV Grid

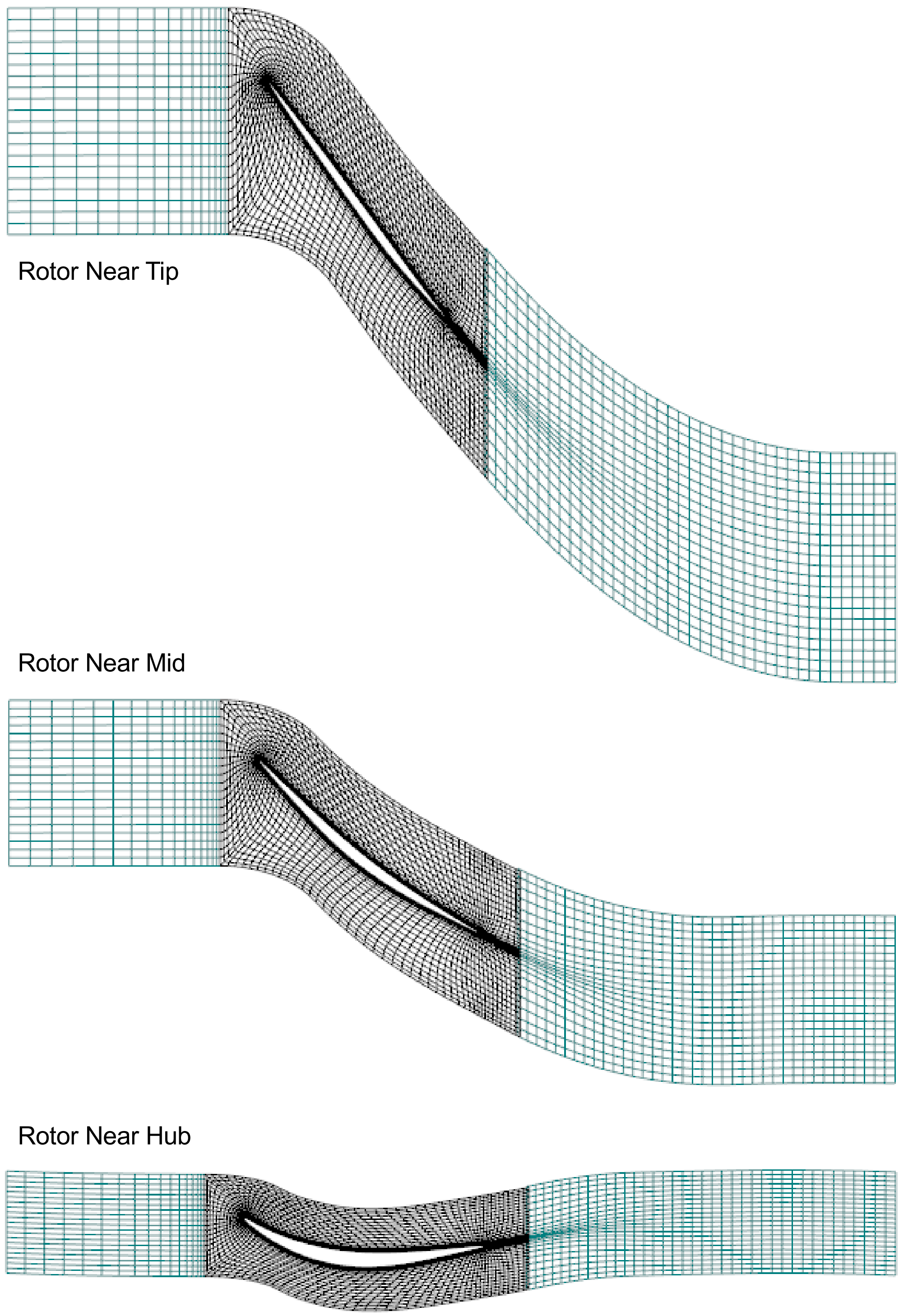

Figure 10: Rotor Grid at Three Spanwise Locations

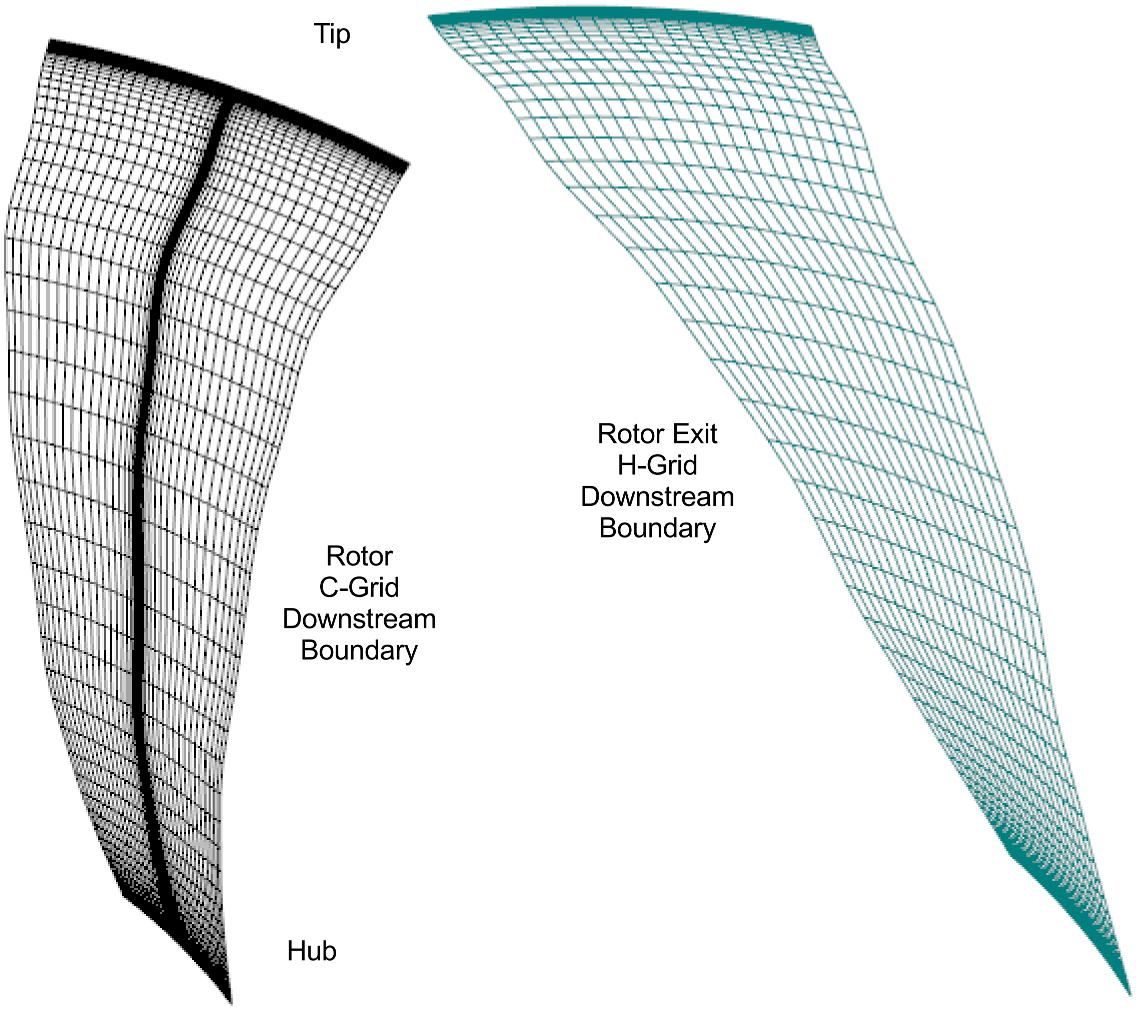

Figure 11: Rotor Grid at Block Downstream Boundaries

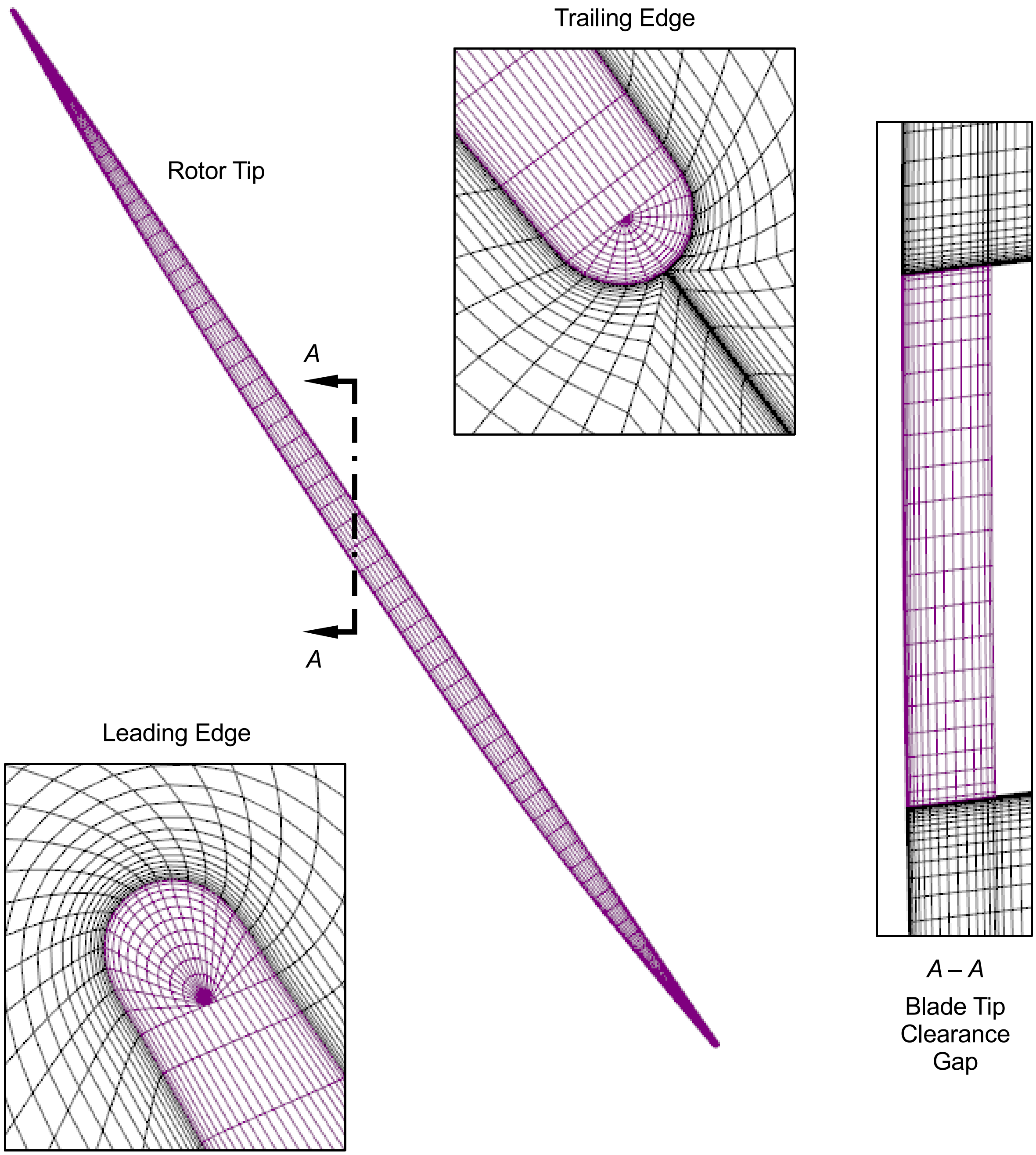

Figure 12: Rotor Tip Clearance Grid

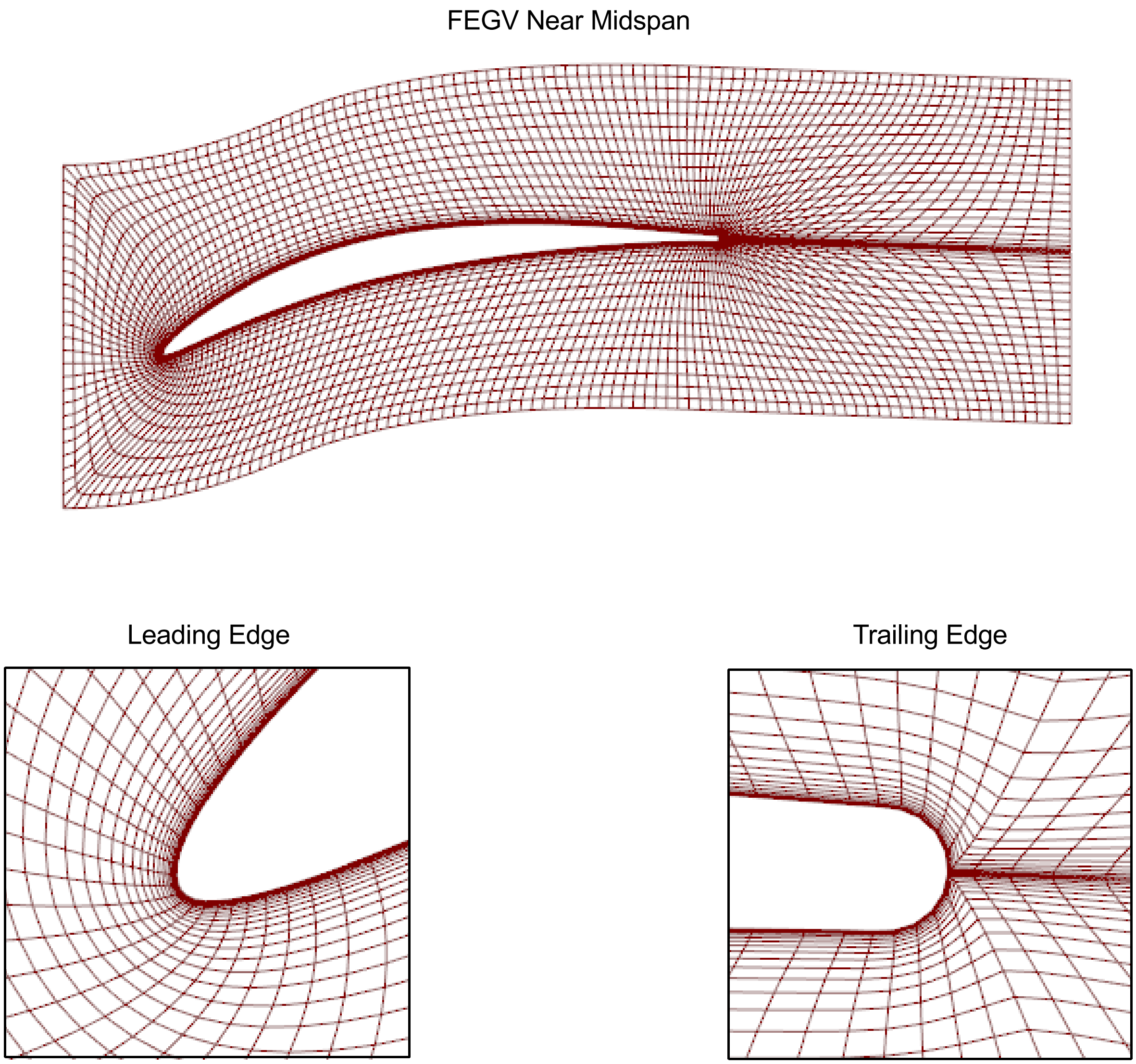

Figure 13: FEGV Grid at Near Midspan Location

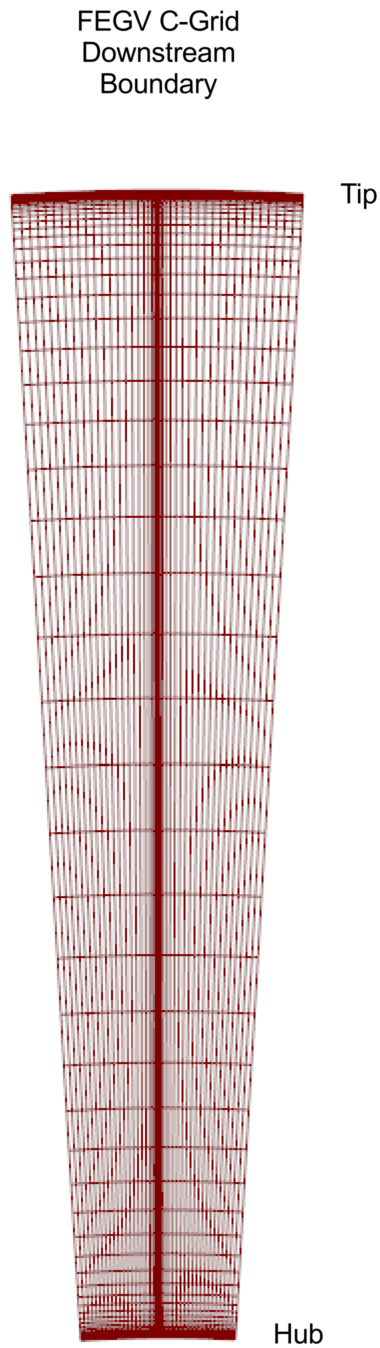

Figure 14: FEGV Grid at Block Downstream Boundary

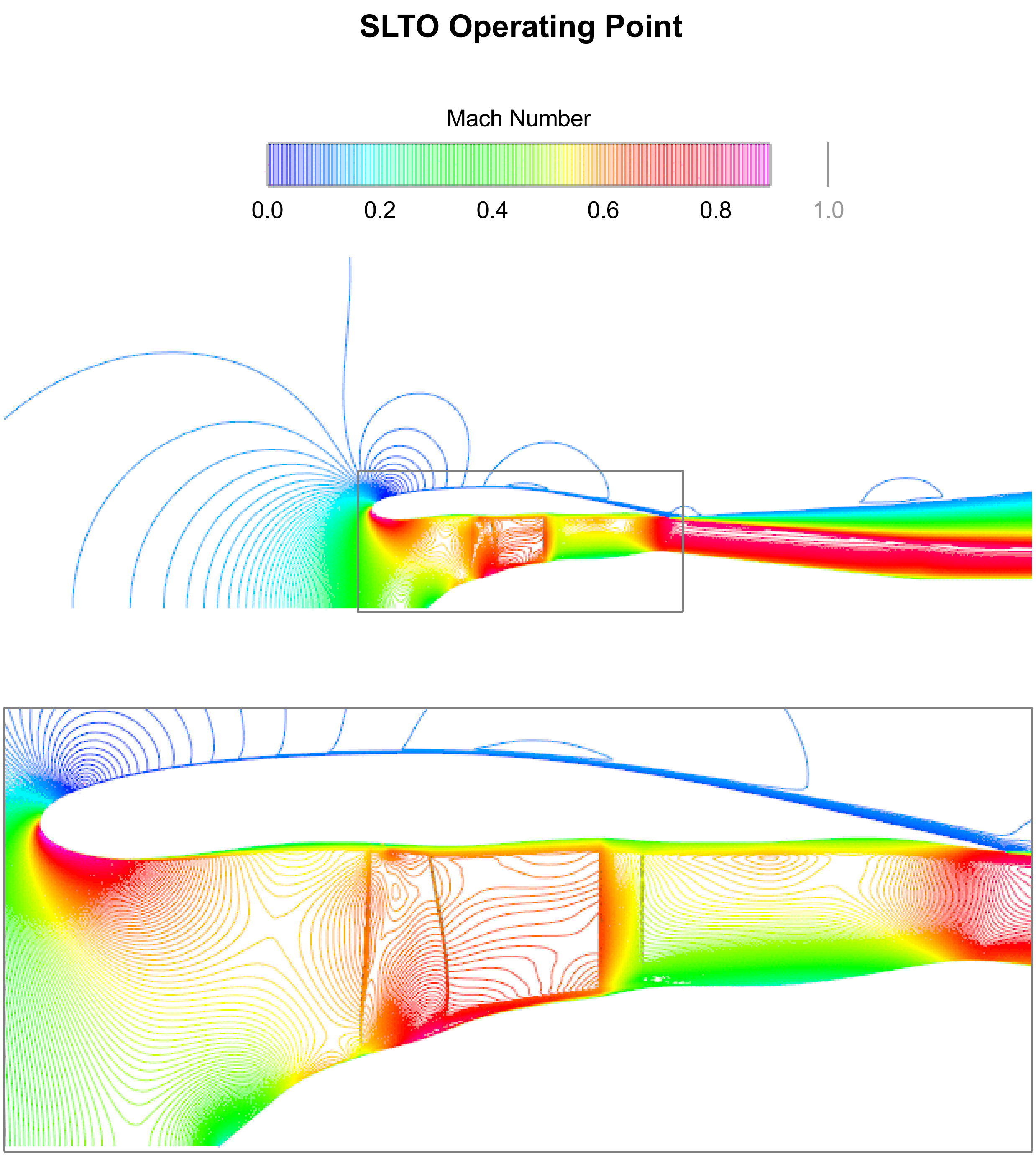

Figure 15: Computed Fan System Flow Field for the SLTO Operating Point; Pitchwise-Averaged Flow; Mach Number Contours

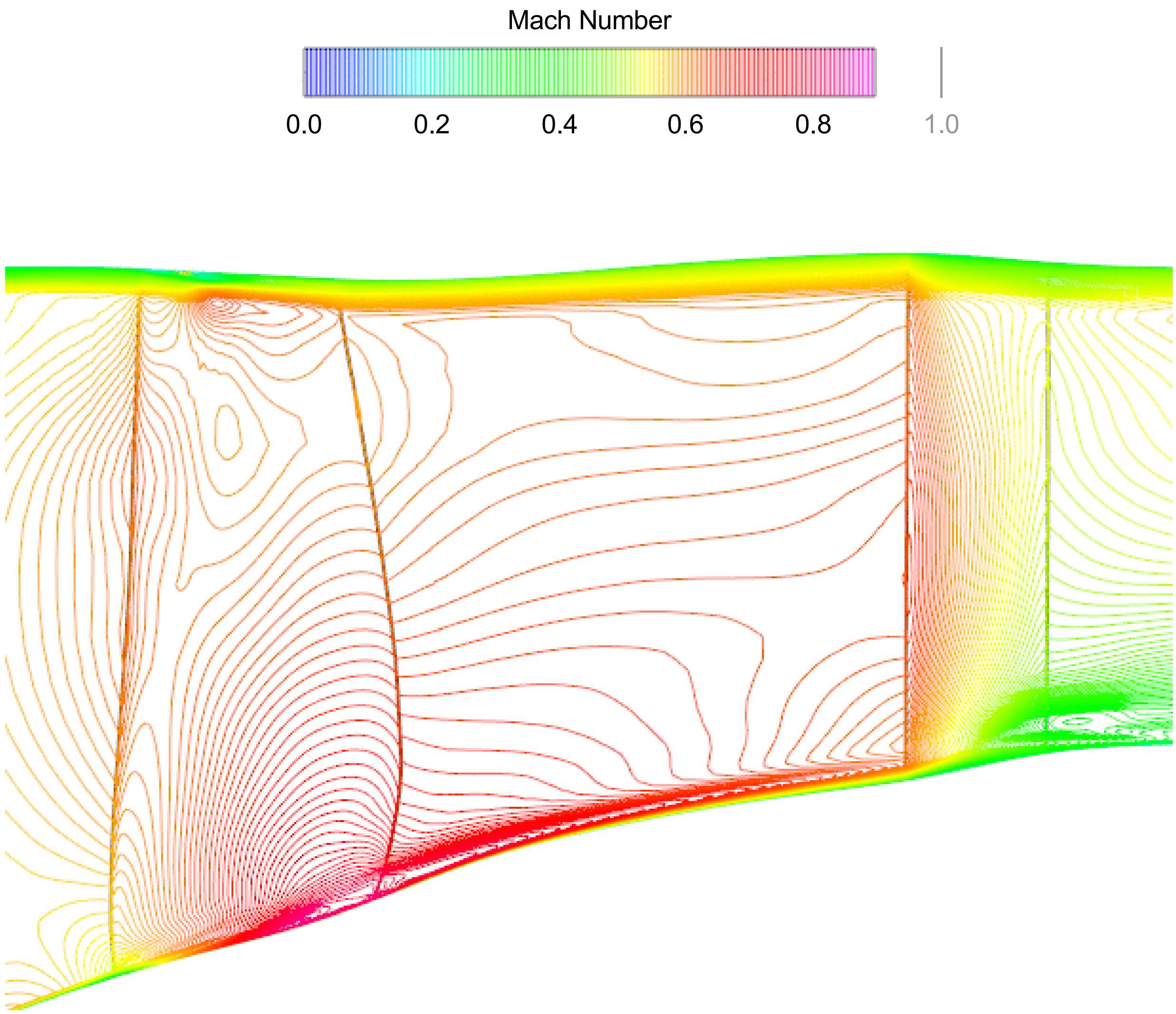

Figure 16: Computed Fan Blade Row Flow Fields for the SLTO Operating Point; Pitchwise-Averaged Flow; Mach Number Contours

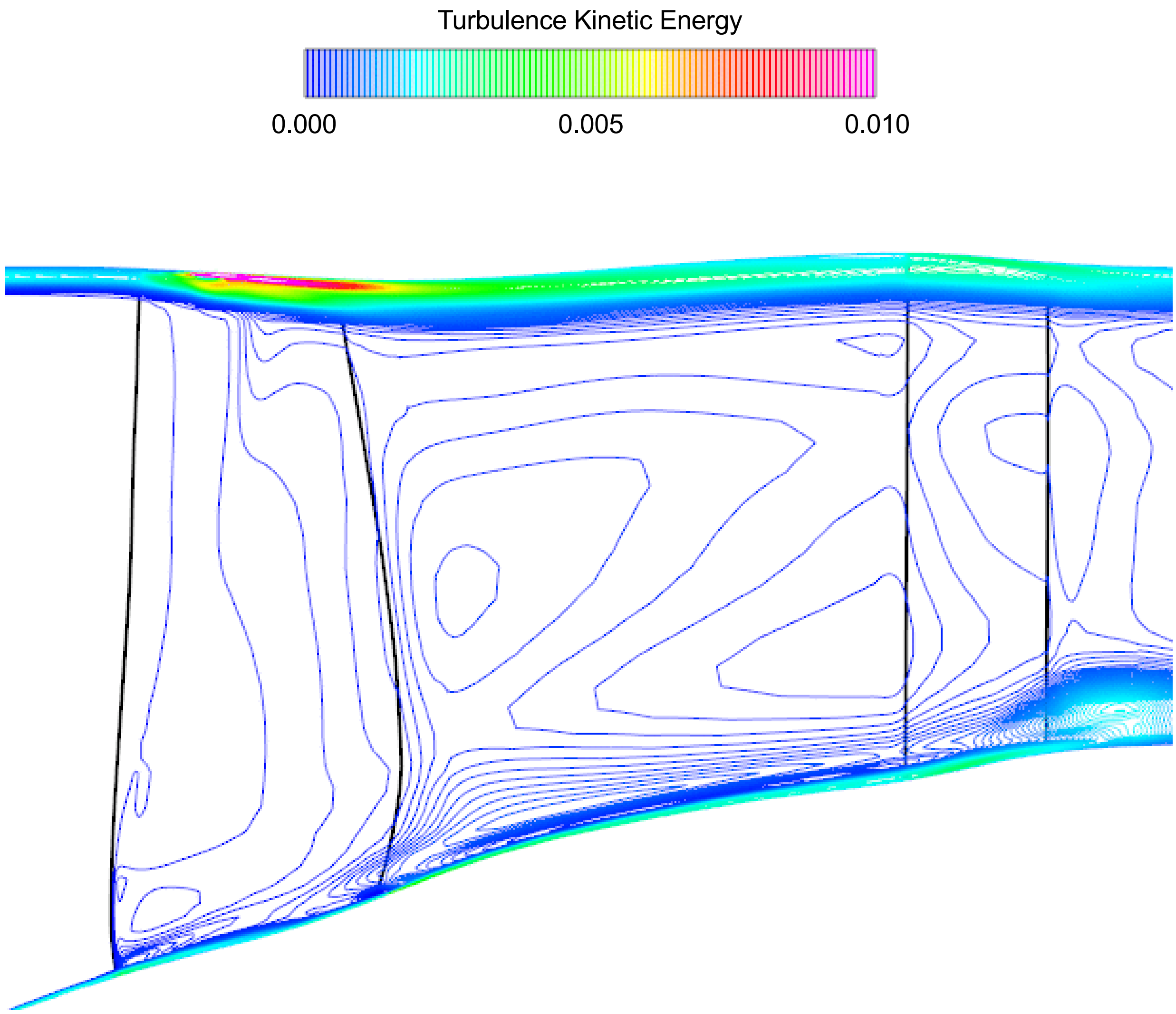

Figure 17: Computed Fan Blade Row Flow Fields for the SLTO Operating Point; Pitchwise-Averaged Flow; Turbulence Kinetic Energy Contours

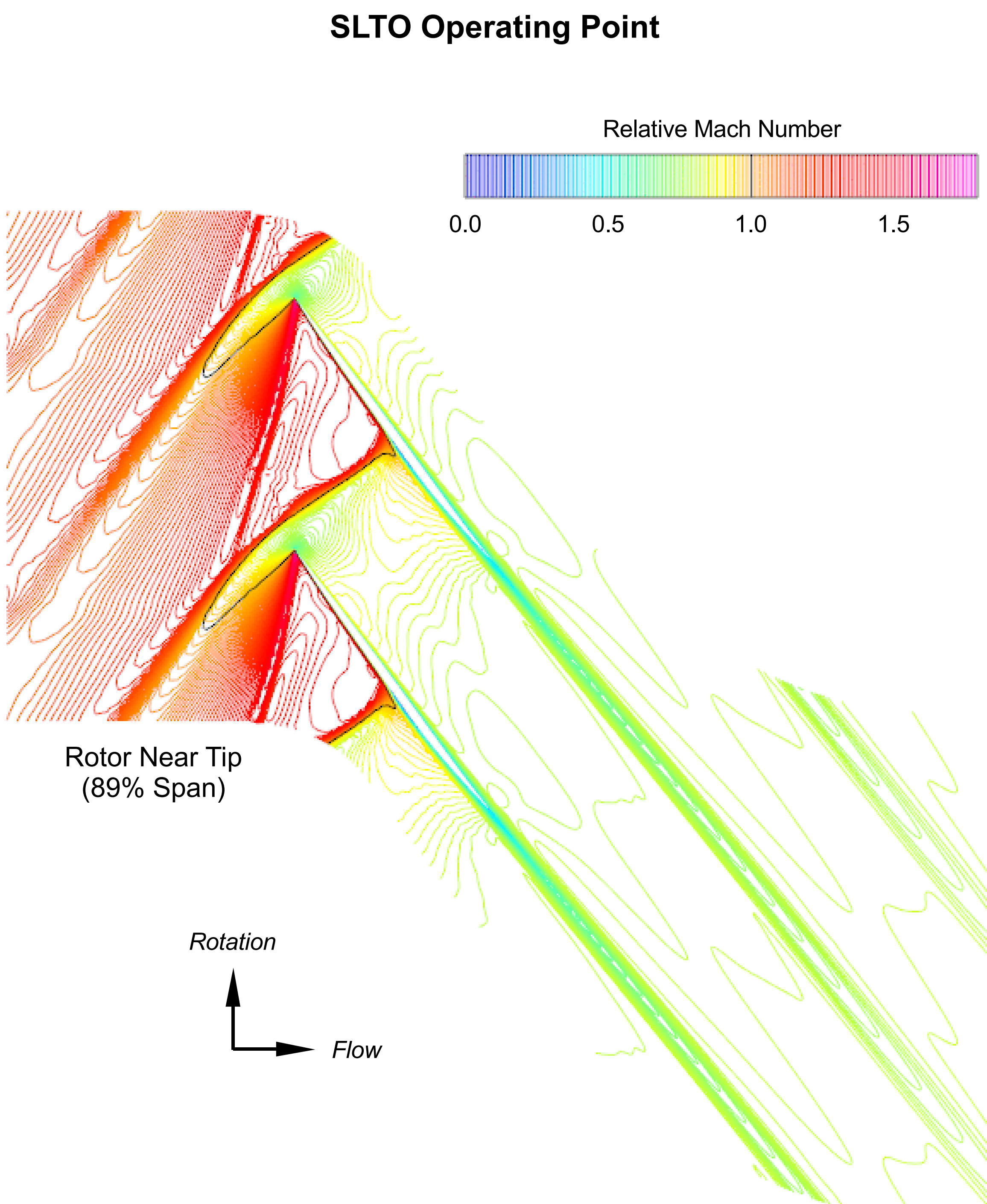

Figure 18a: Computed Rotor Flow Field for the SLTO Operating Point; Blade-to-Blade Relative Mach Number Contours

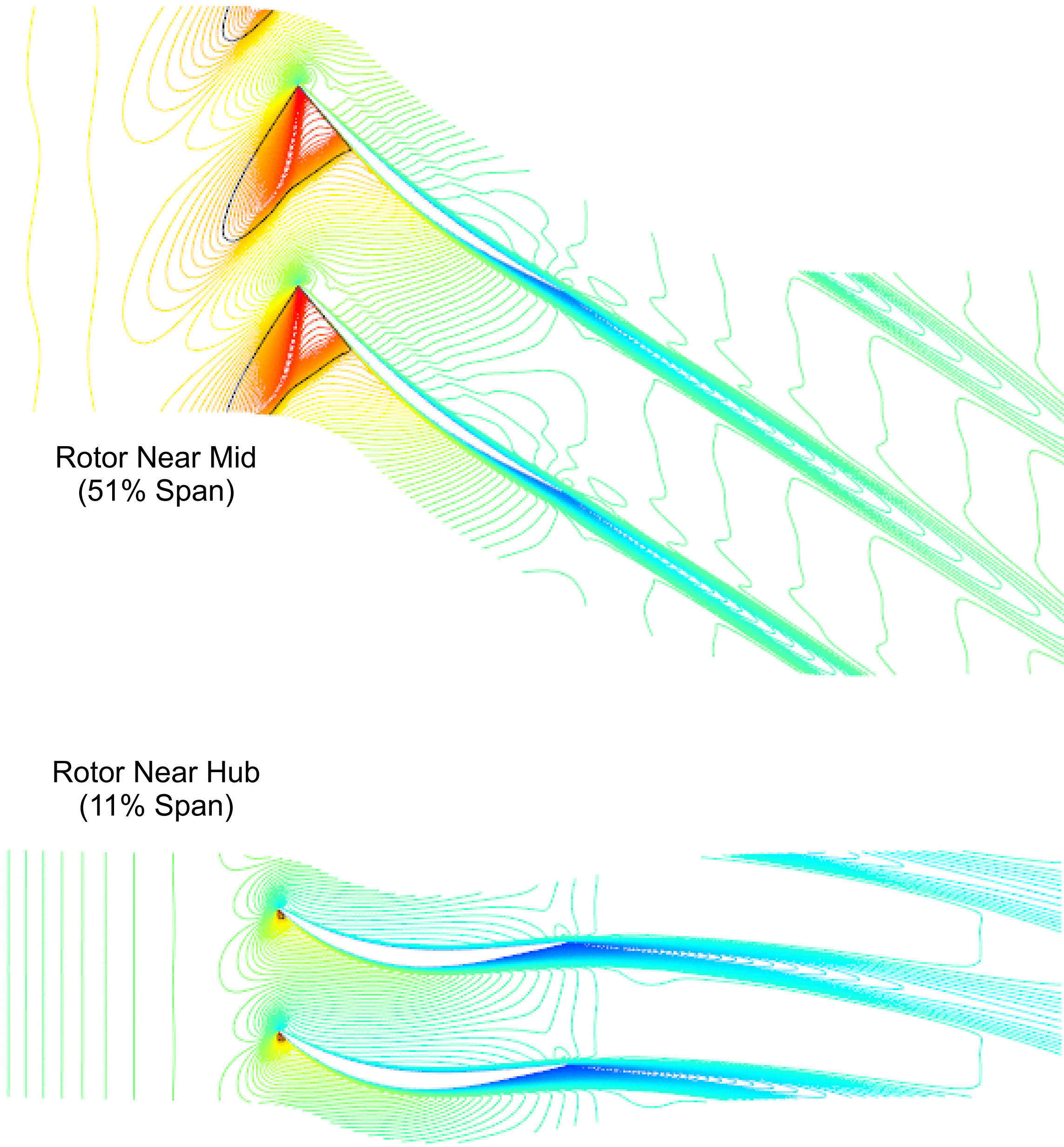

Figure 18b: Computed Rotor Flow Field for the SLTO Operating Point; Blade-to-Blade Relative Mach Number Contours

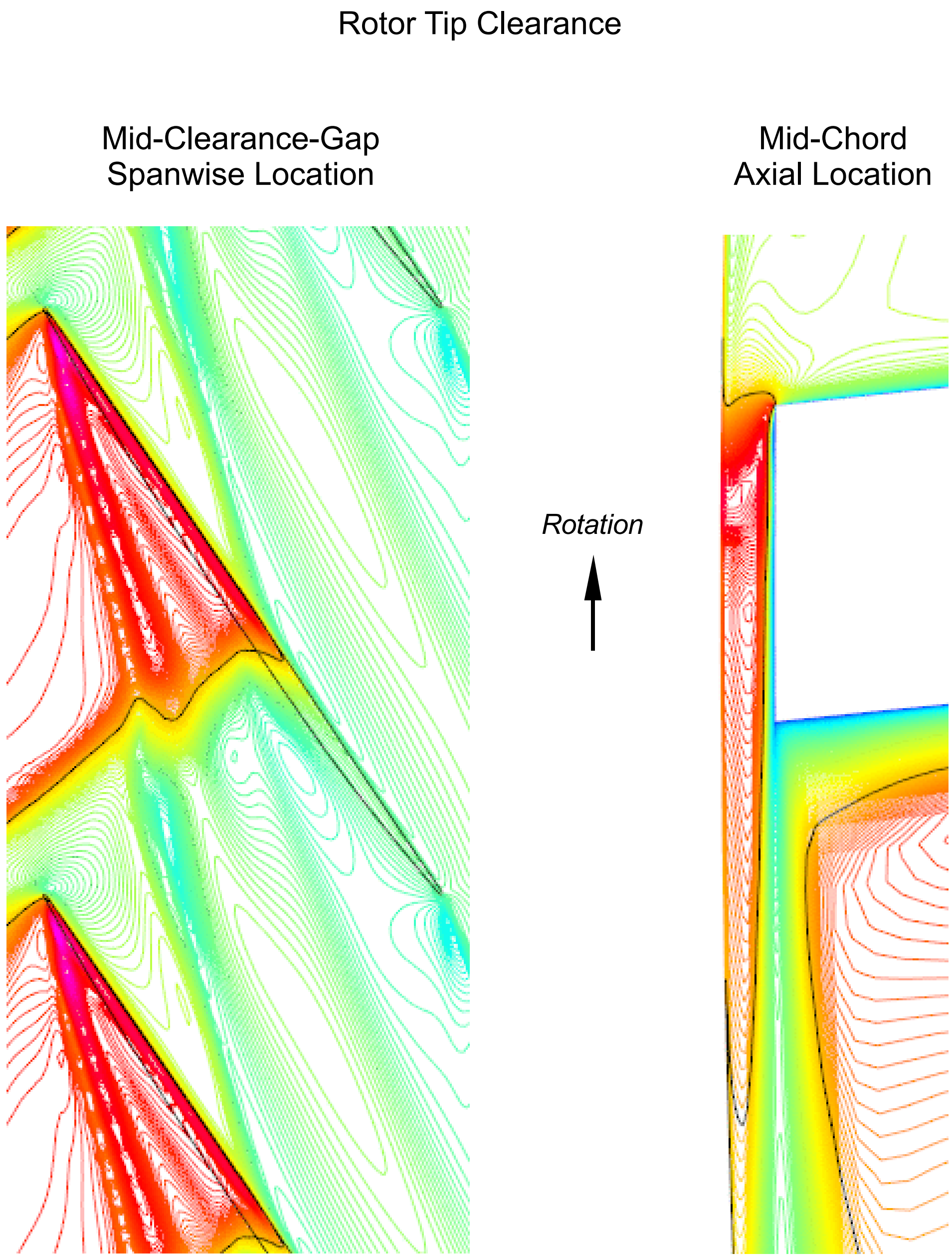

Figure 19: Computed Rotor Tip Flow Field for the SLTO Operating Point; Relative Mach Number Contours (Legend in Figure 18a)

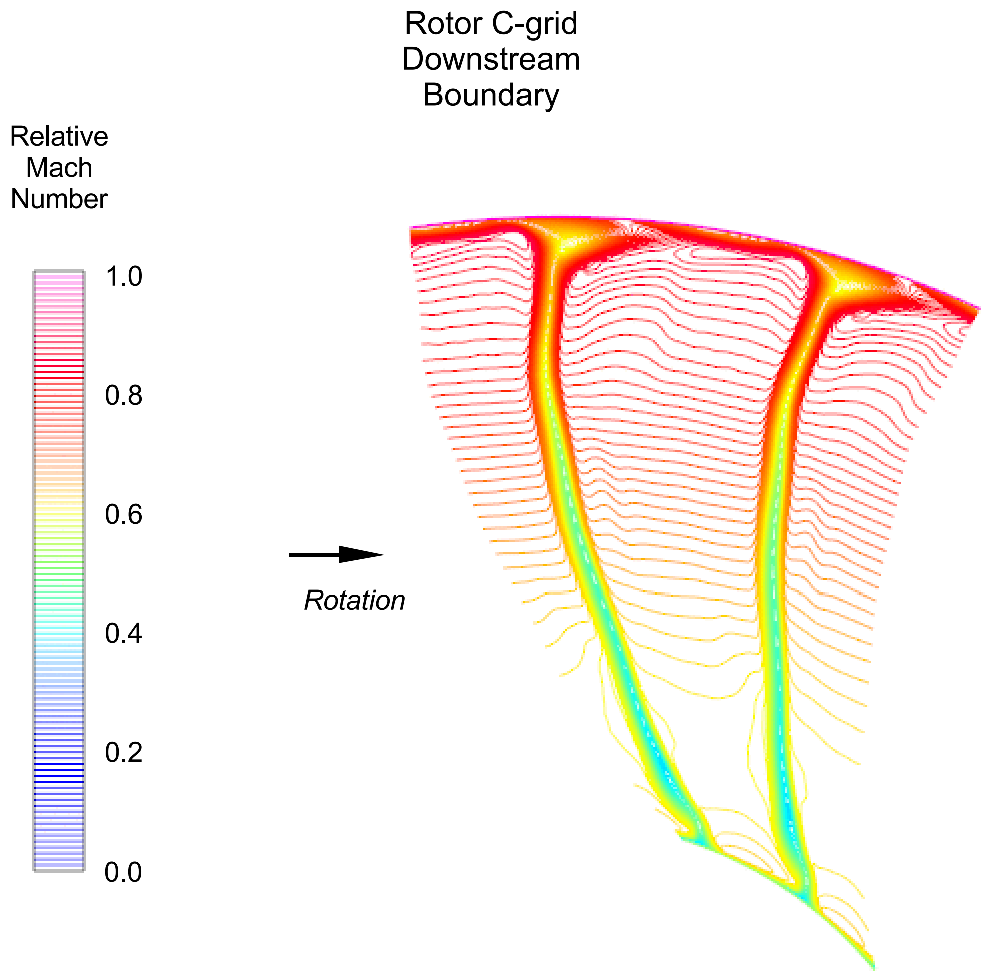

Figure 20: Computed Rotor Flow Field for the SLTO Operating Point; Downstream Boundary of C-Grid; Relative Mach Number Contours

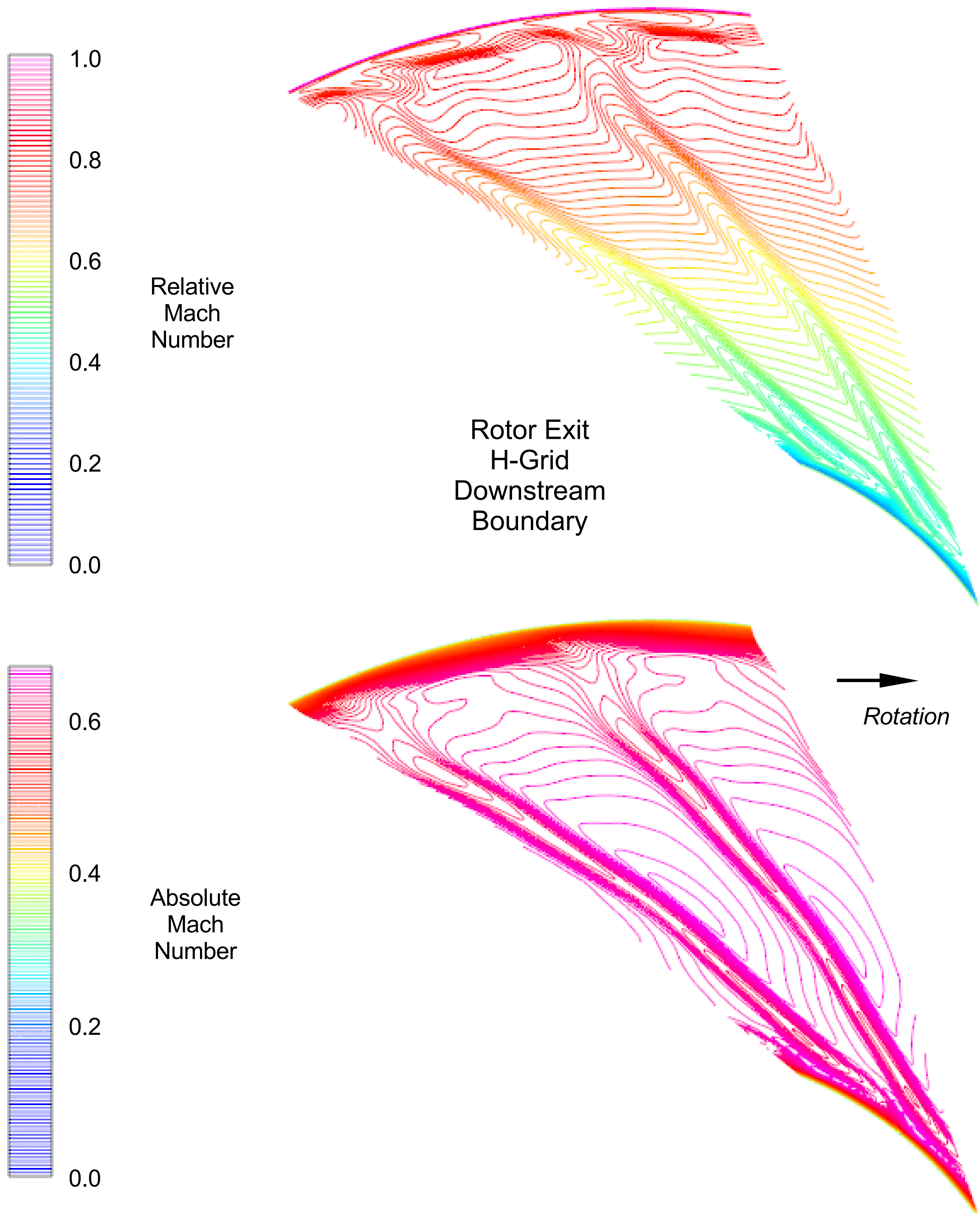

Figure 21a: Computed Rotor Flow Field for the SLTO Operating Point; Downstream Mixing Plane; Relative and Absolute Mach Number Contours

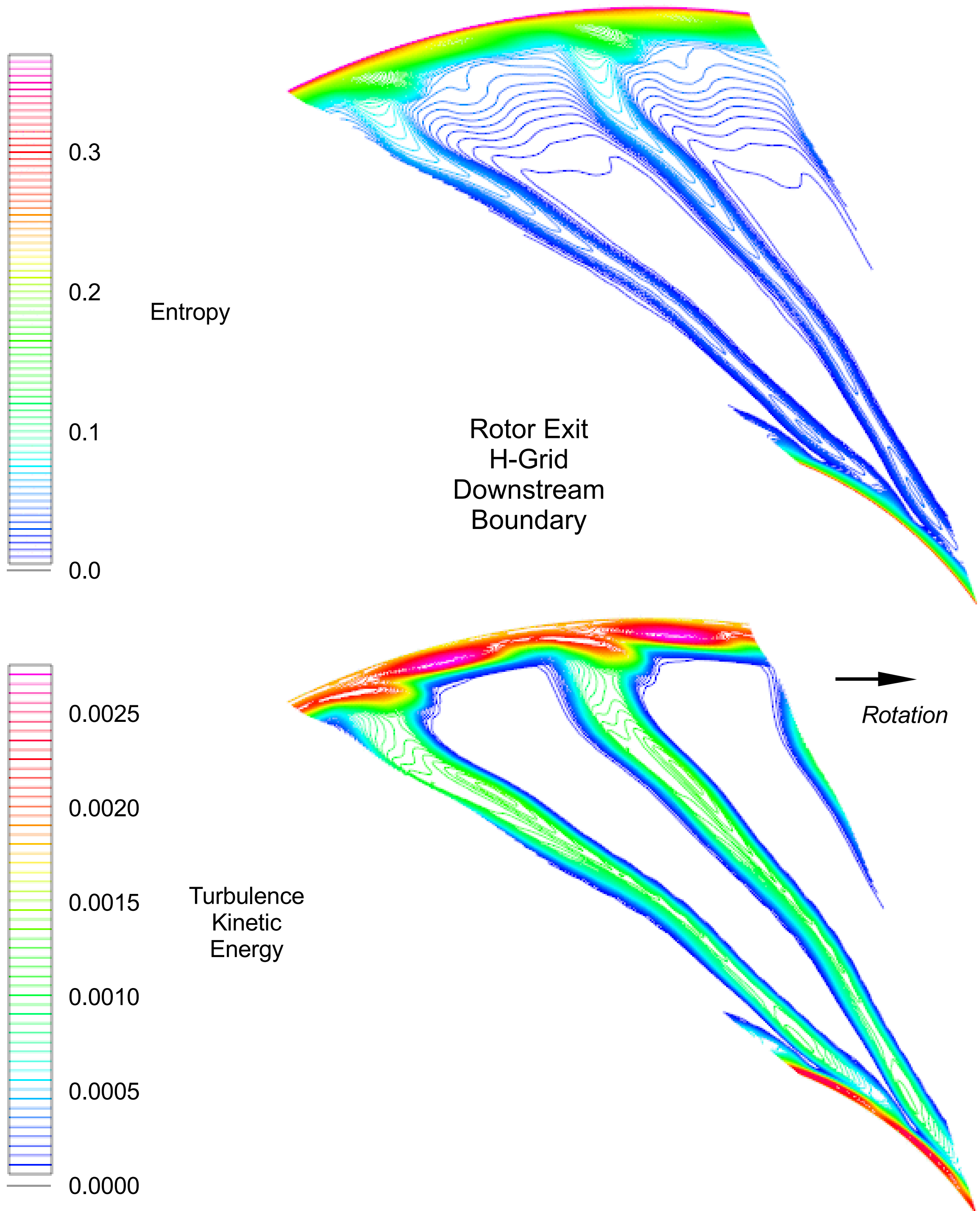

Figure 21b: Computed Rotor Flow Field for the SLTO Operating Point; Downstream Mixing Plane; Entropy and Turbulence Kinetic Energy Contours

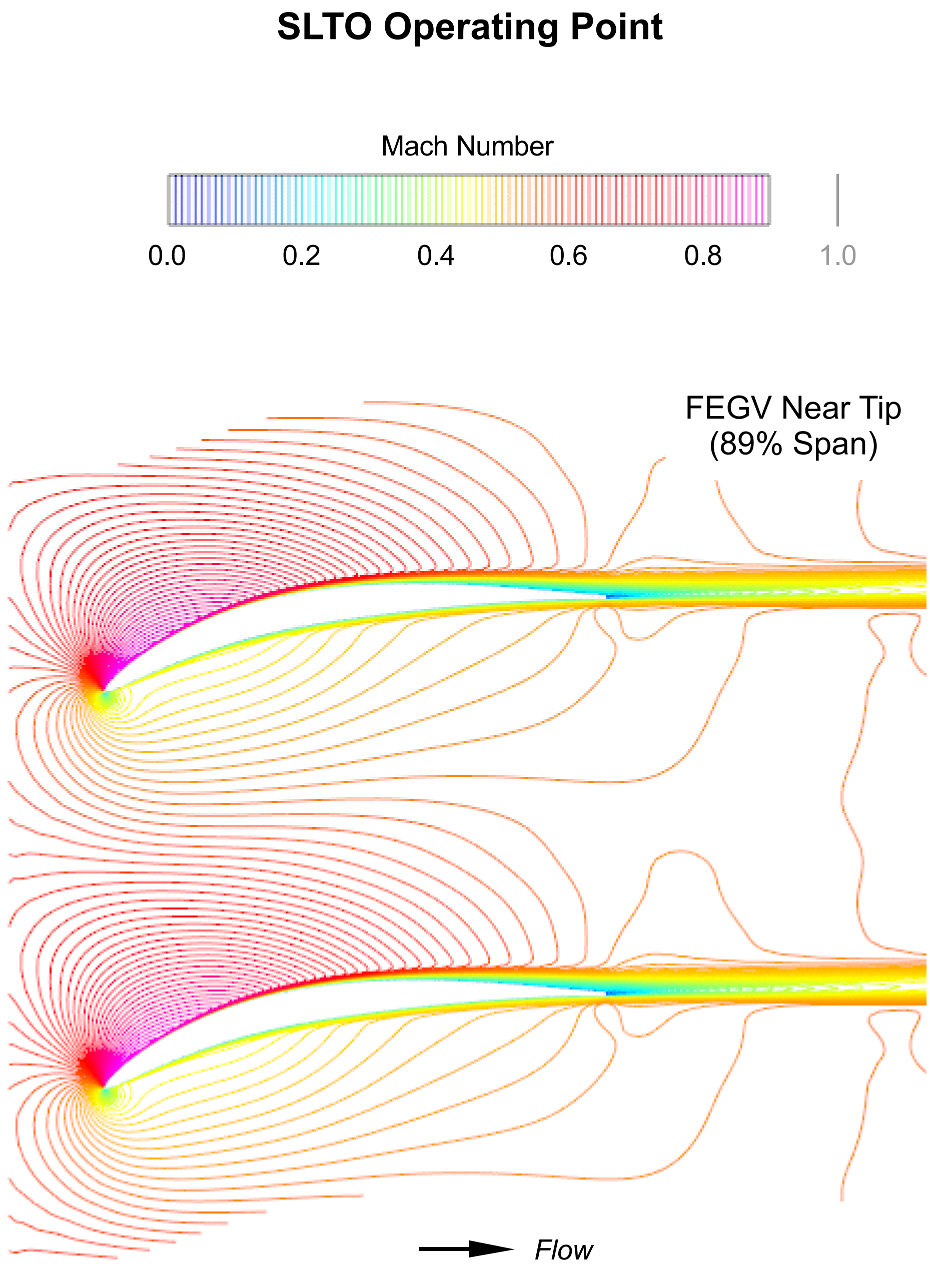

Figure 22a: Computed FEGV Flow Field for the SLTO Operating Point; Blade-to-Blade Mach Number Contours

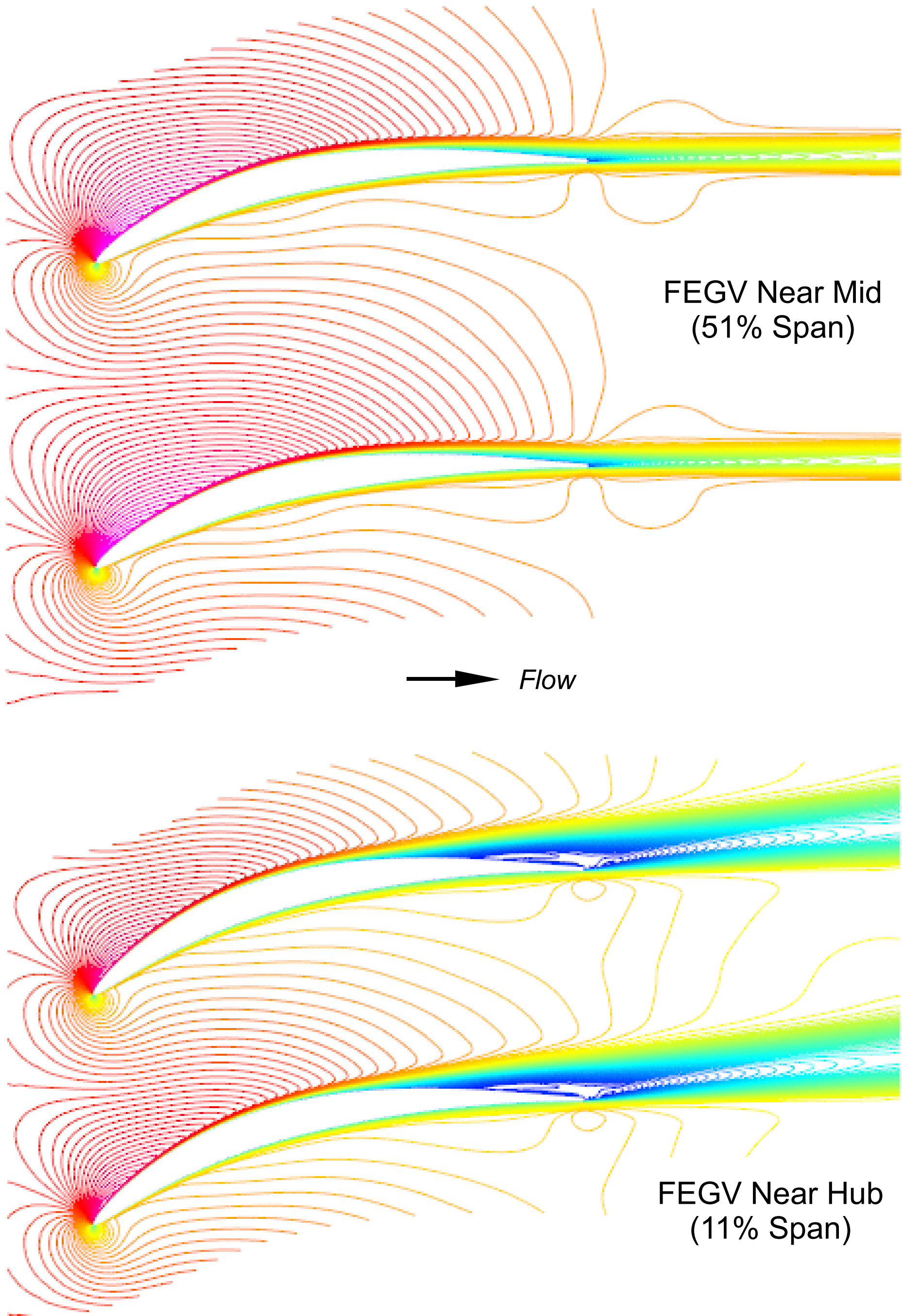

Figure 22b: Computed FEGV Flow Field for the SLTO Operating Point; Blade-to-Blade Mach Number Contours

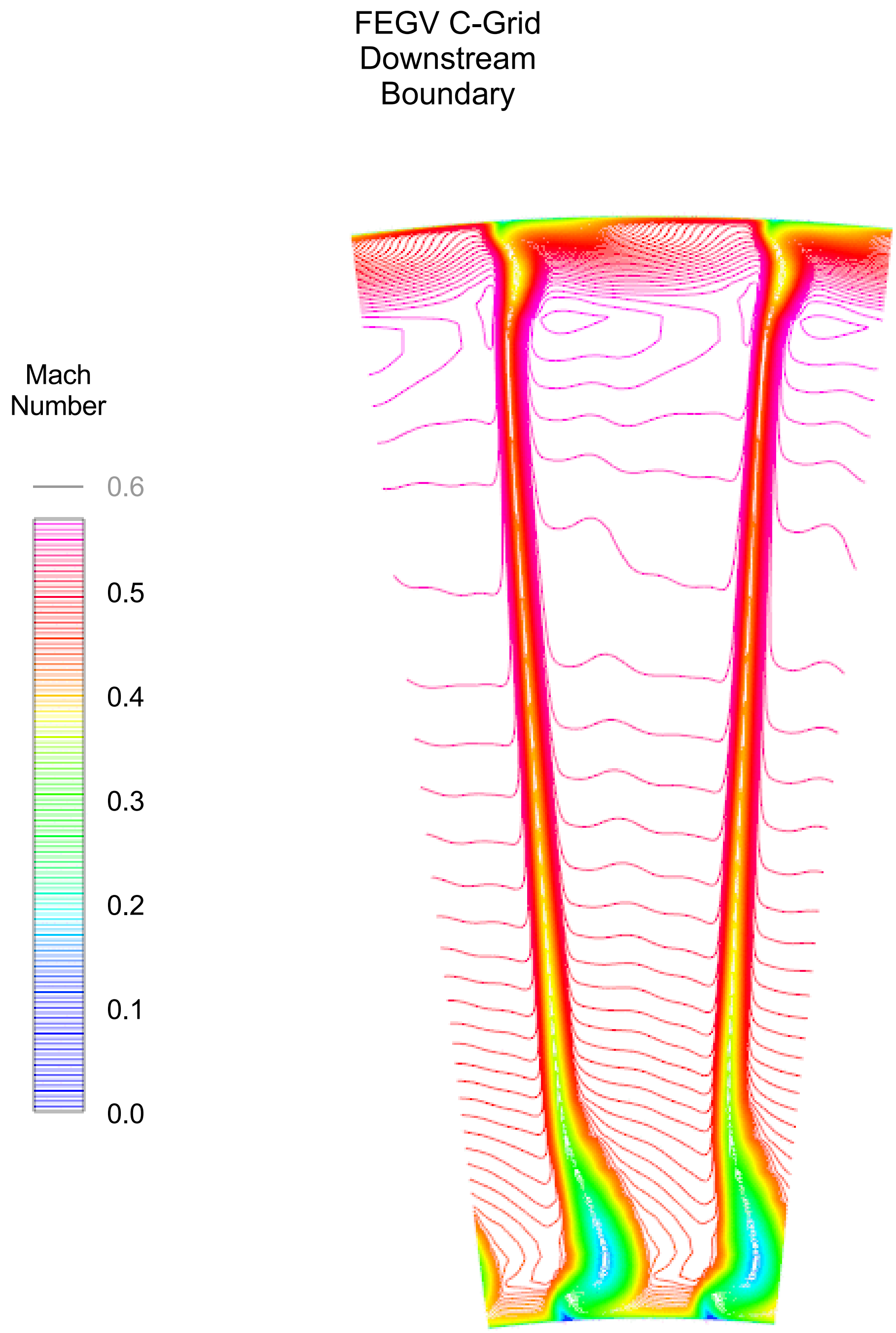

Figure 23: Computed FEGV Flow Field for the SLTO Operating Point; Downstream Mixing Plane; Mach Number Contours

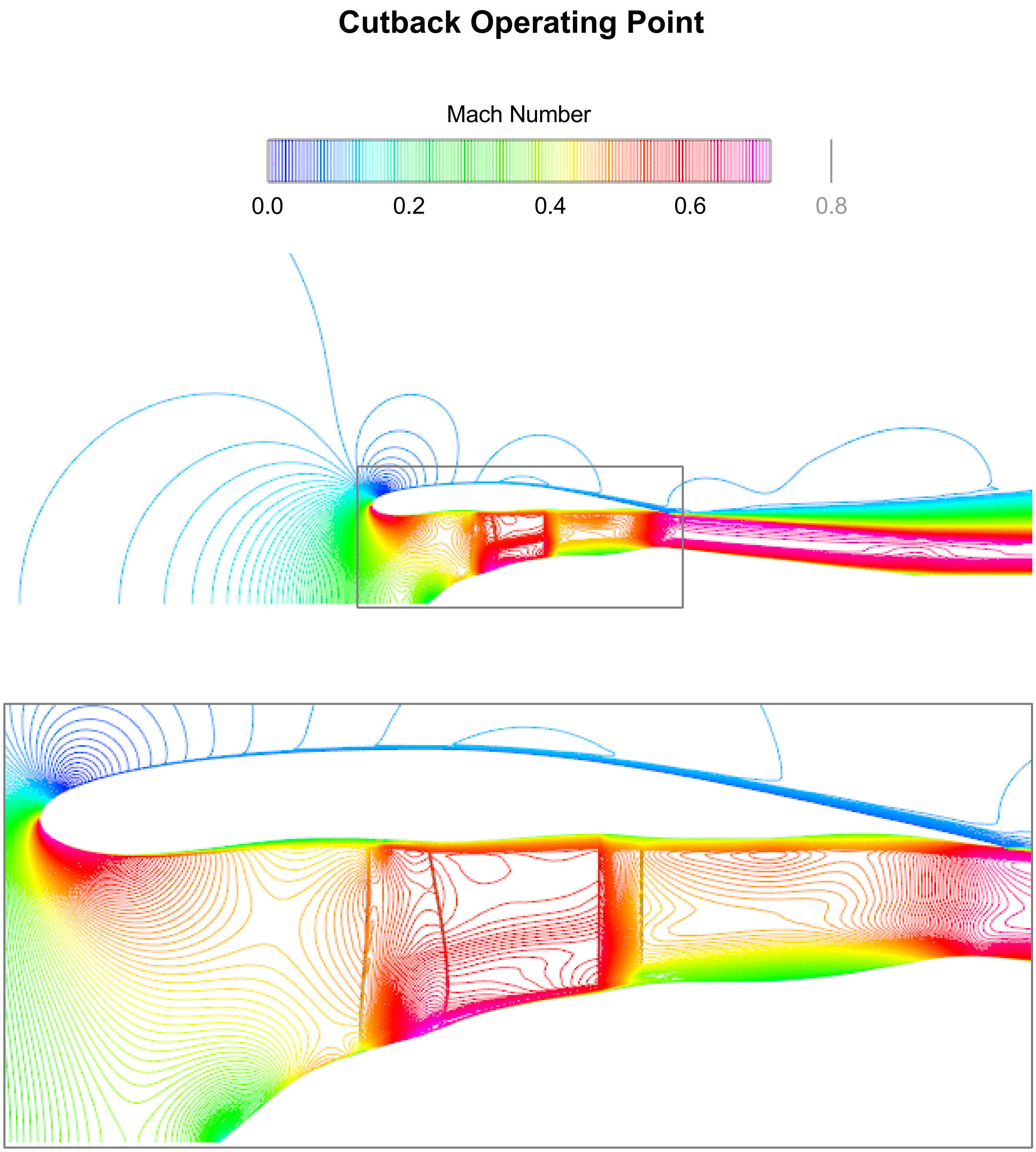

Figure 24: Computed Fan System Flow Field for the Cutback Operating Point; Pitchwise-Averaged Flow; Mach Number Contours

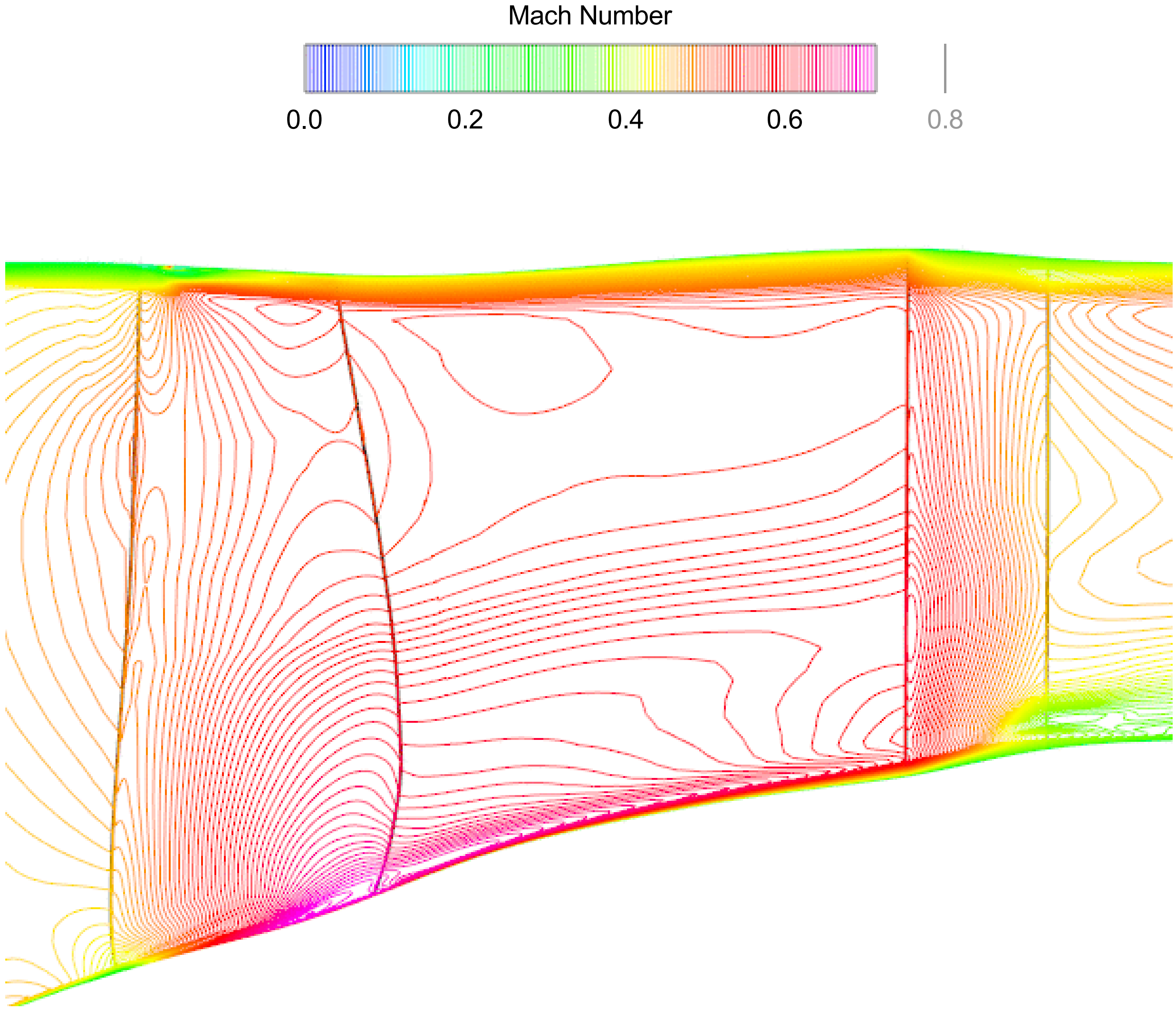

Figure 25: Computed Fan Blade Row Flow Fields for the Cutback Operating Point; Pitchwise-Averaged Flow; Mach Number Contours

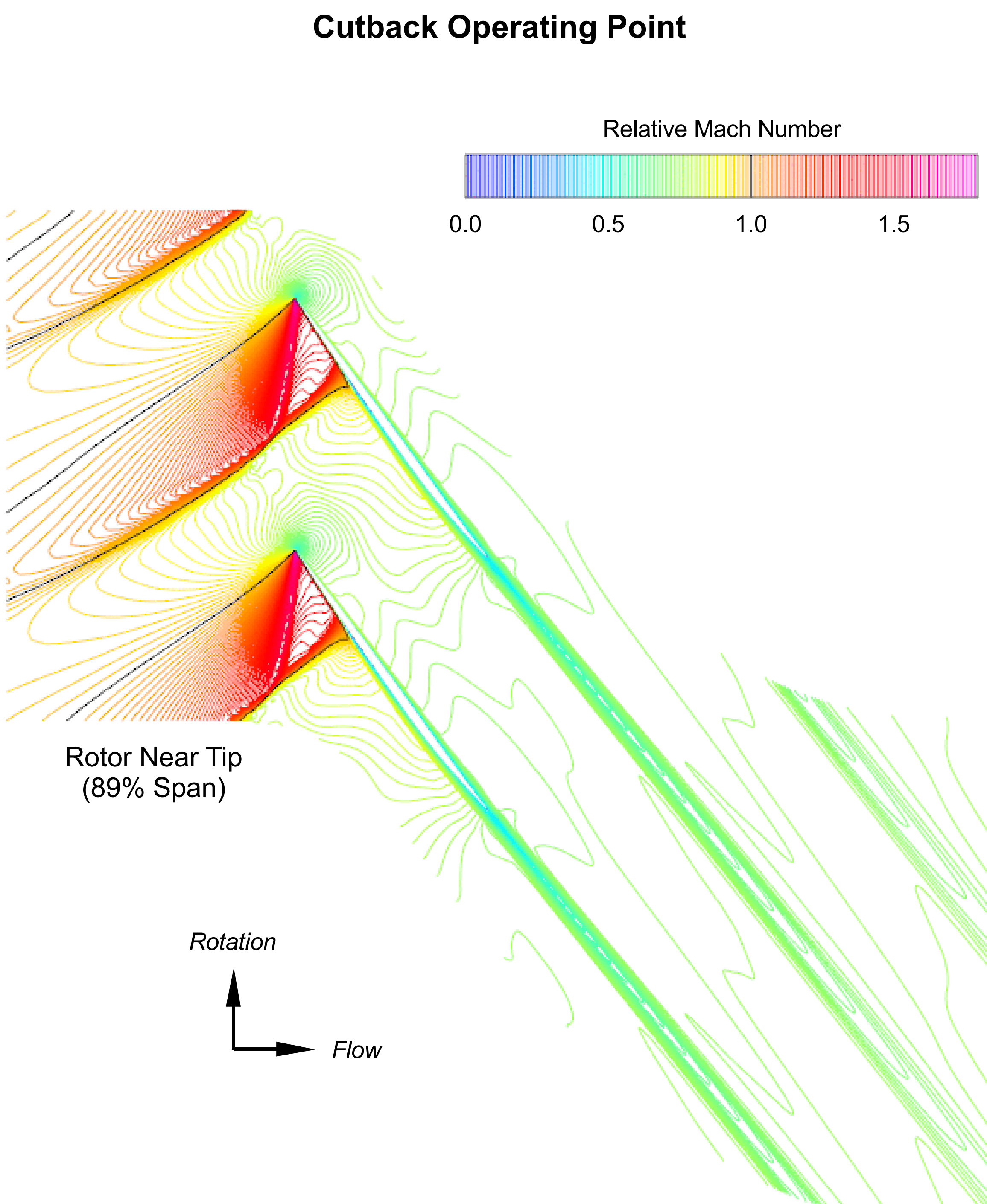

Figure 26a: Computed Rotor Flow Field for the Cutback Operating Point; Blade-to-Blade Relative Mach Number Contours

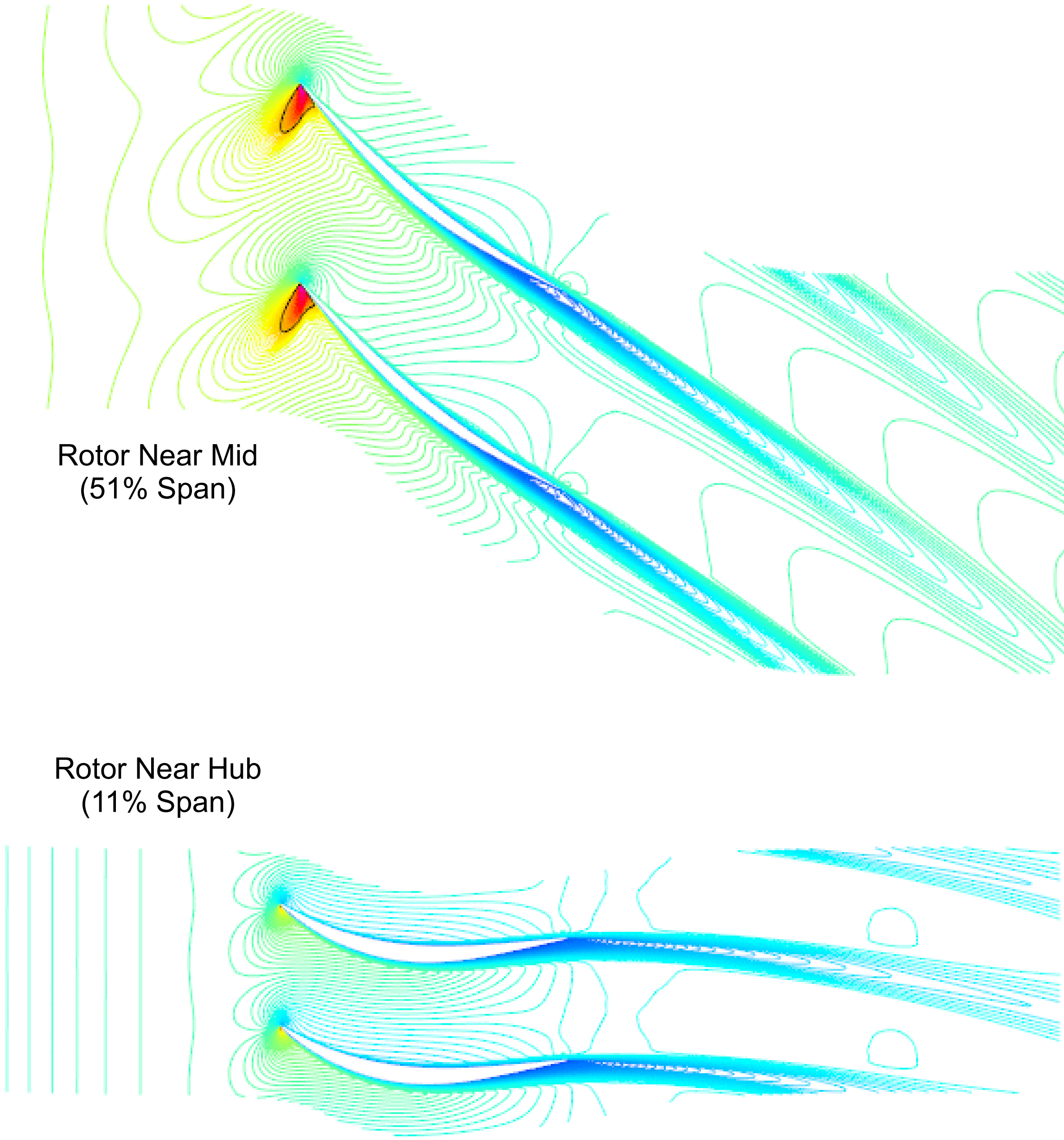

Figure 26b: Computed Rotor Flow Field for the Cutback Operating Point; Blade-to-Blade Relative Mach Number Contours

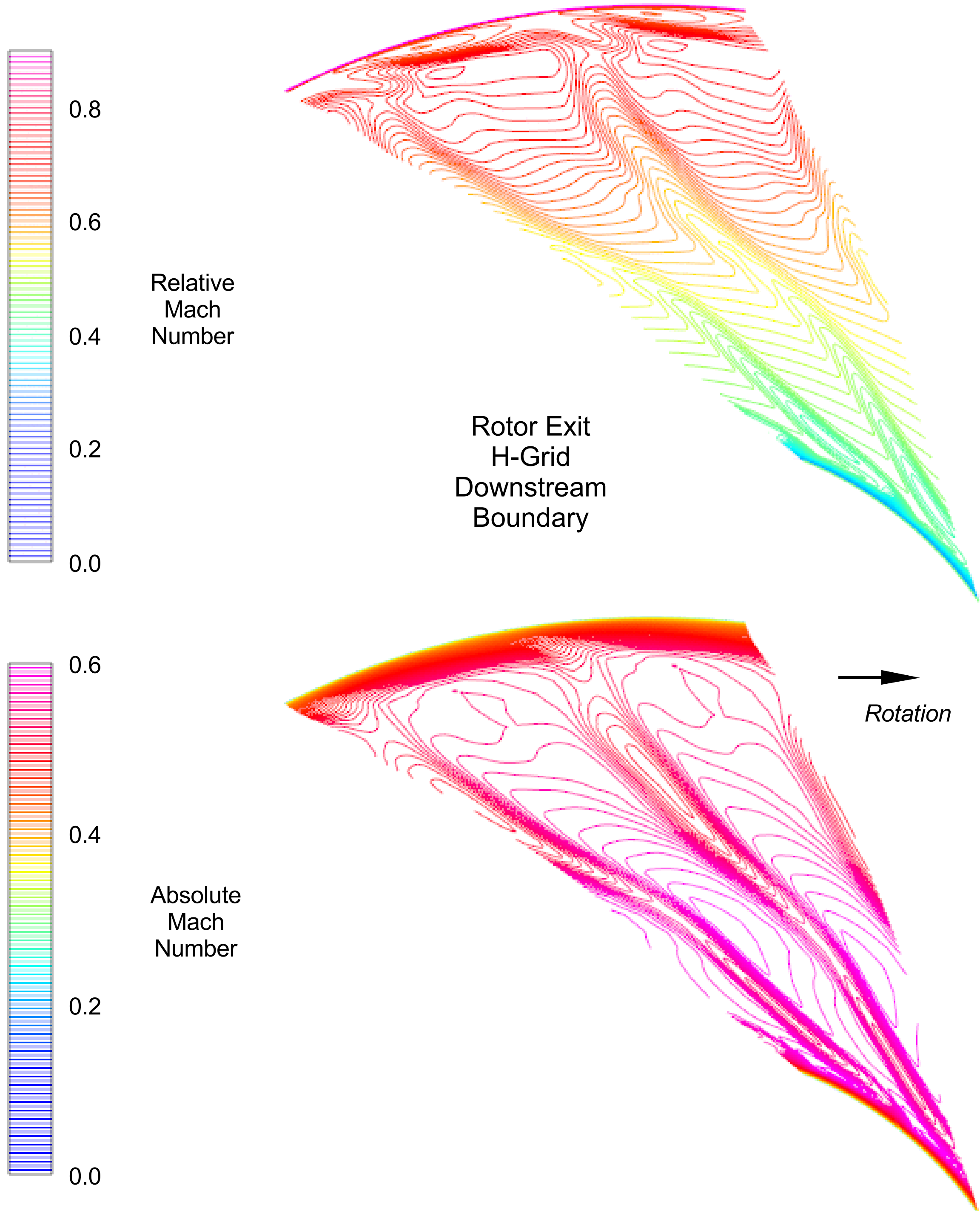

Figure 27a: Computed Rotor Flow Field for the Cutback Operating Point; Downstream Mixing Plane; Relative and Absolute Mach Number Contours

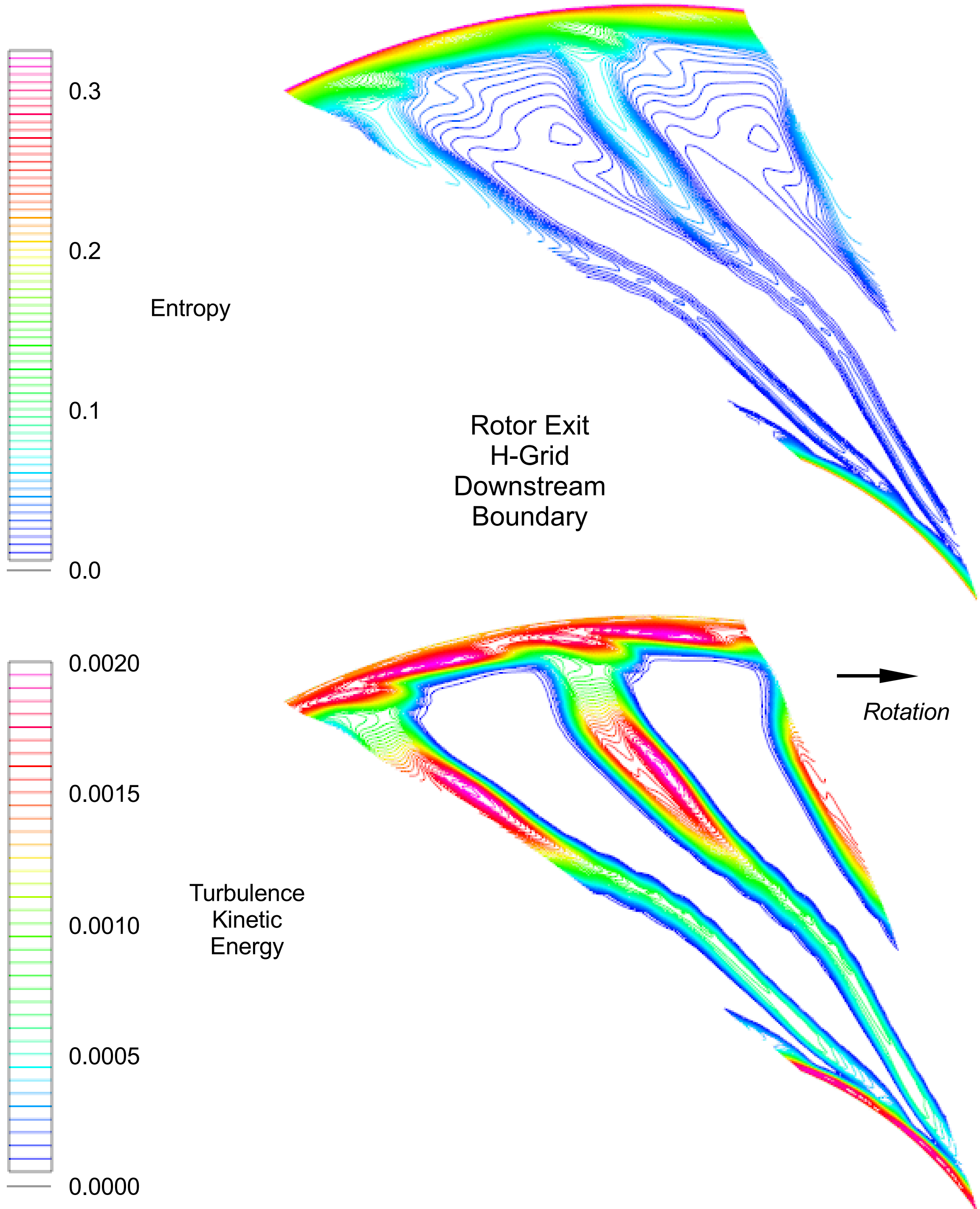

Figure 27b: Computed Rotor Flow Field for the Cutback Operating Point; Downstream Mixing Plane; Entropy and Turbulence Kinetic Energy Contours

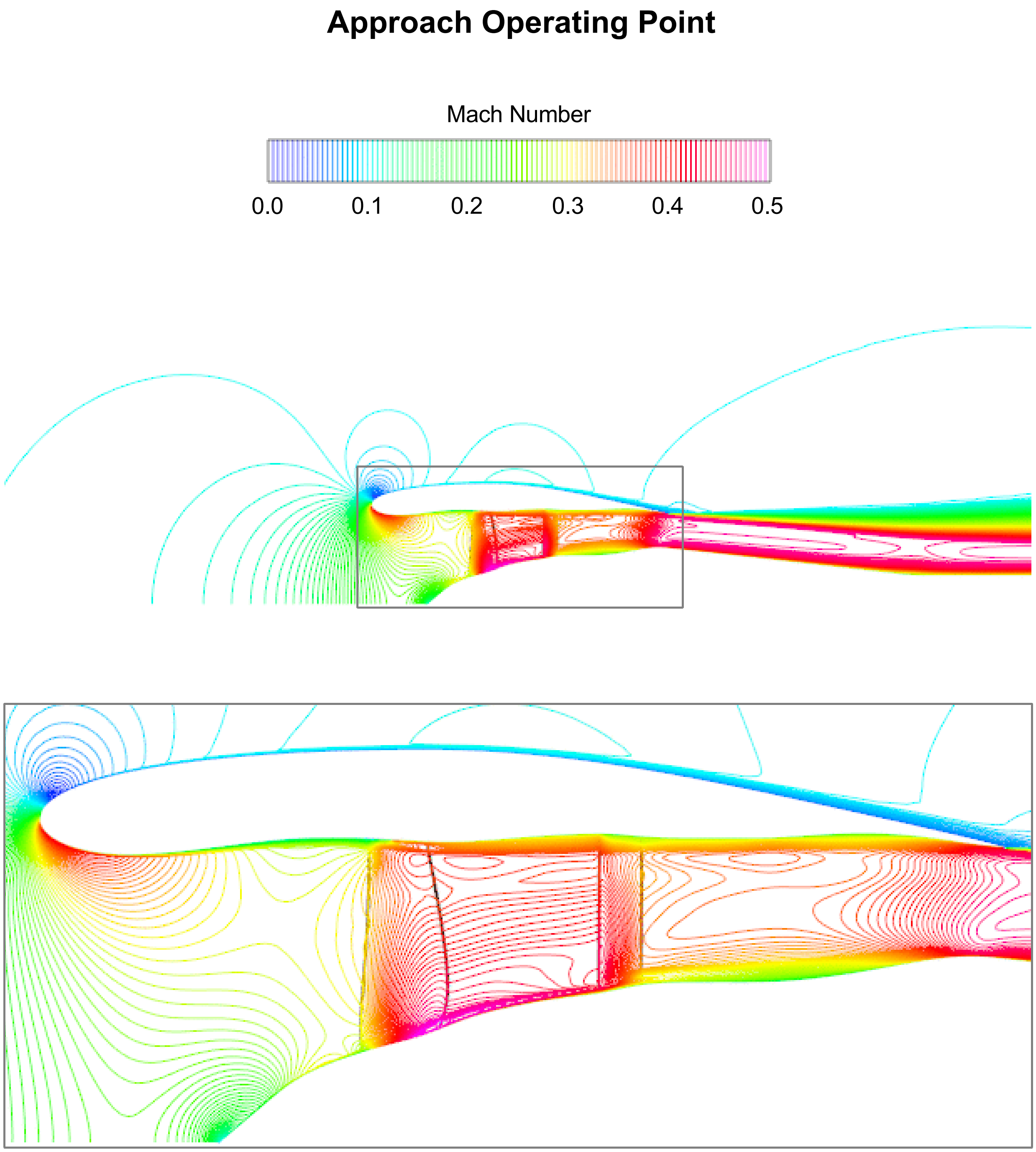

Figure 28: Computed Fan System Flow Field for the Approach Operating Point; Pitchwise-Averaged Flow; Mach Number Contours

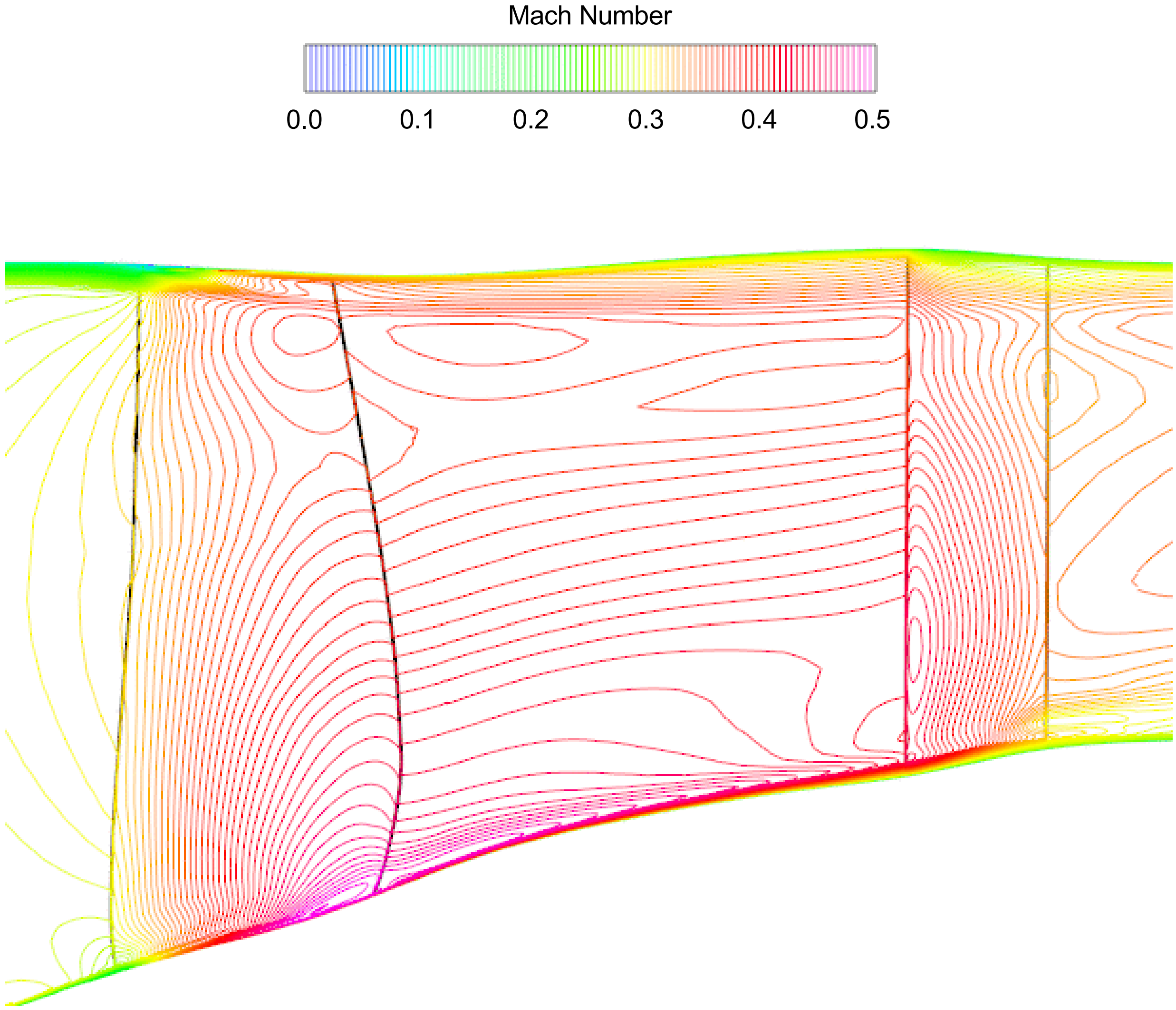

Figure 29: Computed Fan Blade Row Flow Fields for the Approach Operating Point; Pitchwise-Averaged Flow; Mach Number Contours

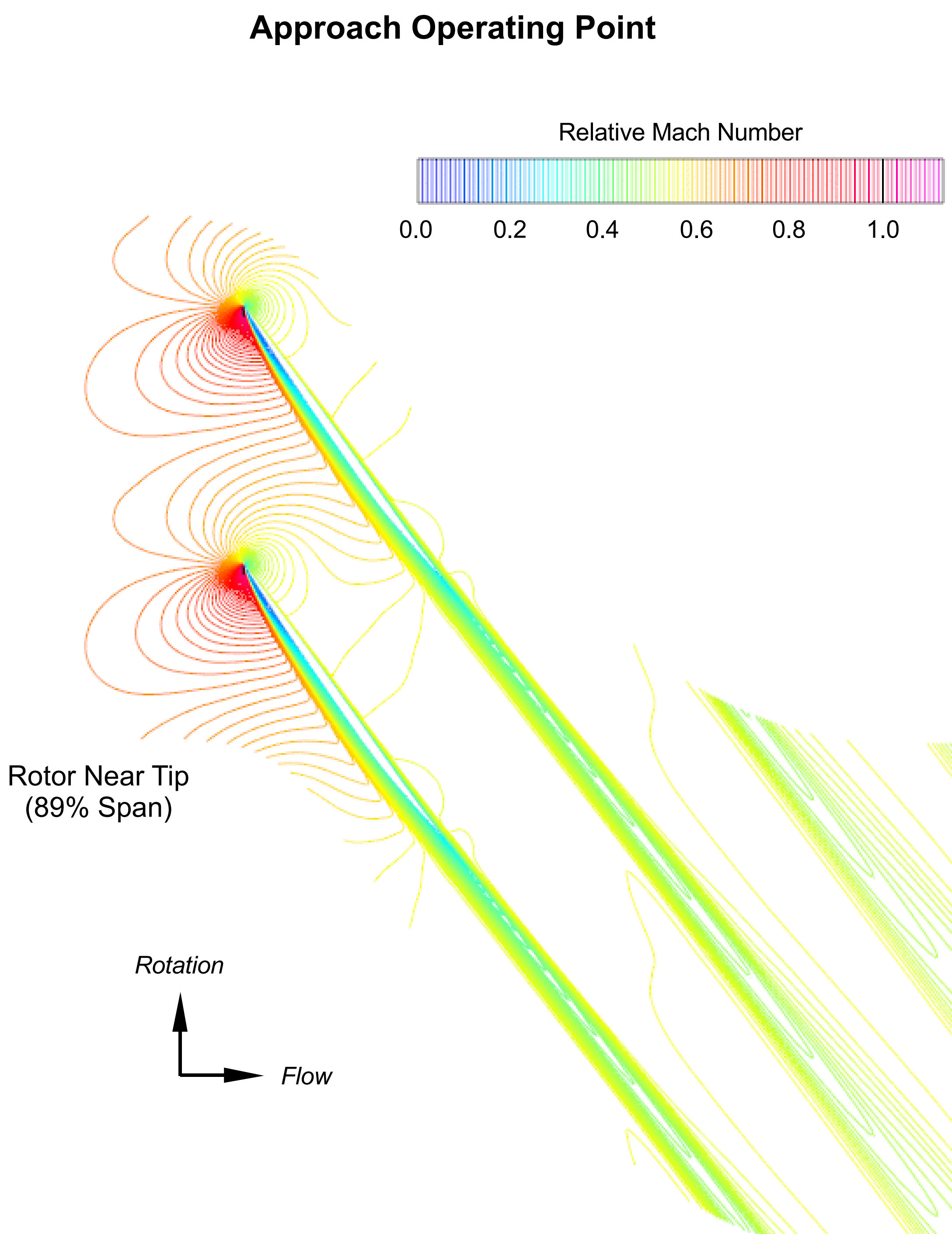

Figure 30a: Computed Rotor Flow Field for the Approach Operating Point; Blade-to-Blade Relative Mach Number Contours

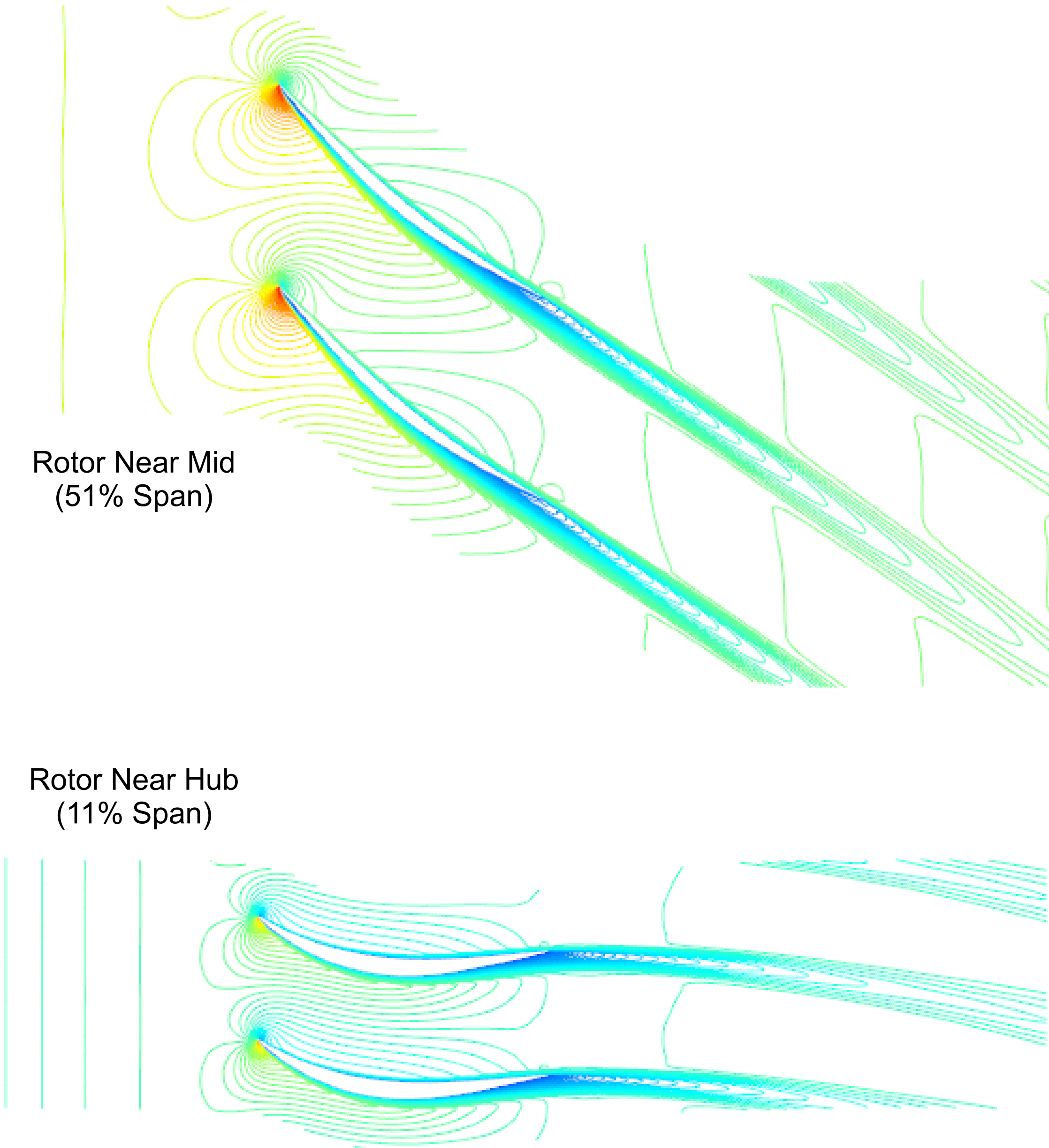

Figure 30b: Computed Rotor Flow Field for the Approach Operating Point; Blade-to-Blade Relative Mach Number Contours

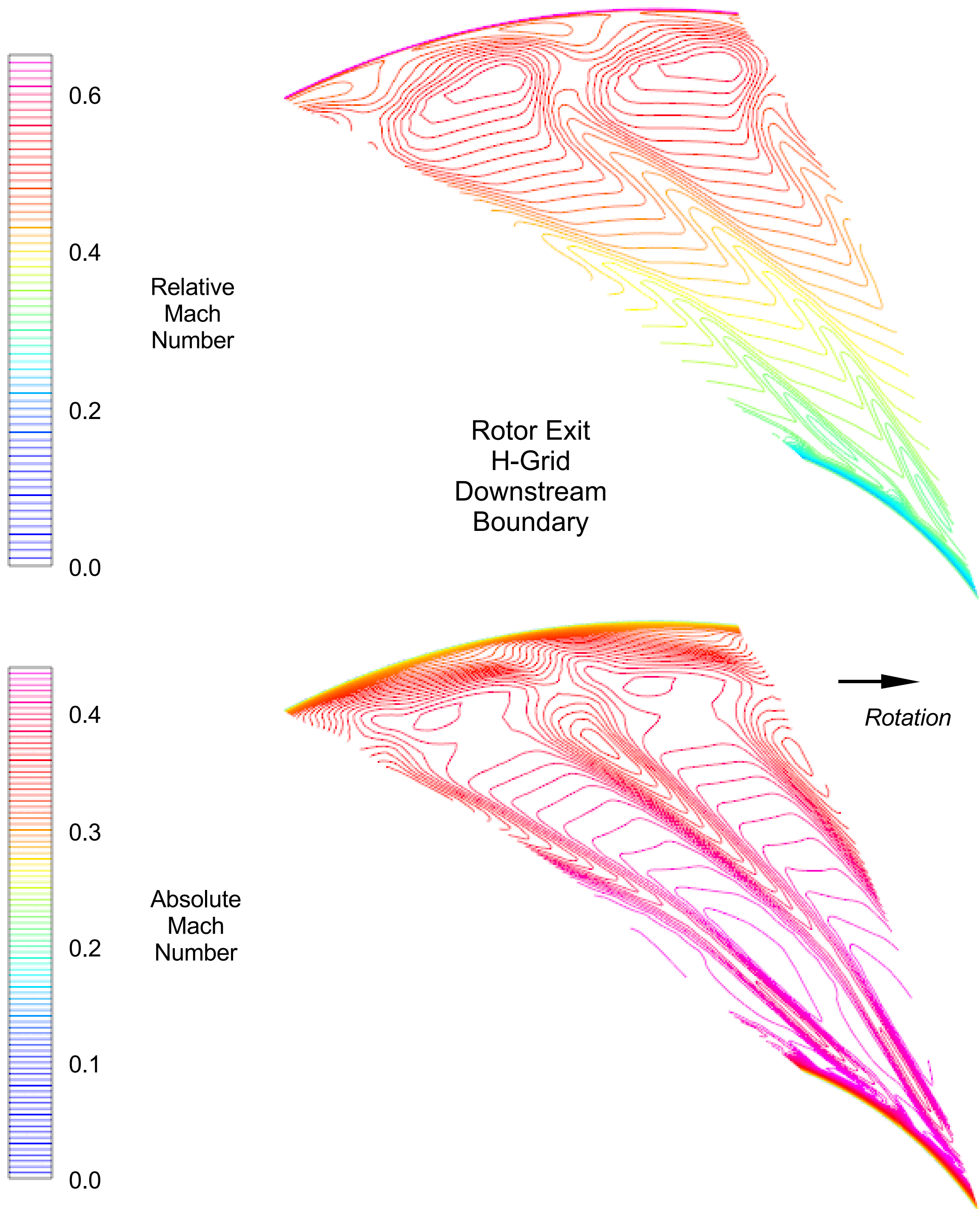

Figure 31a: Computed Rotor Flow Field for the Approach Operating Point; Downstream Mixing Plane; Relative and Absolute Mach Number Contours

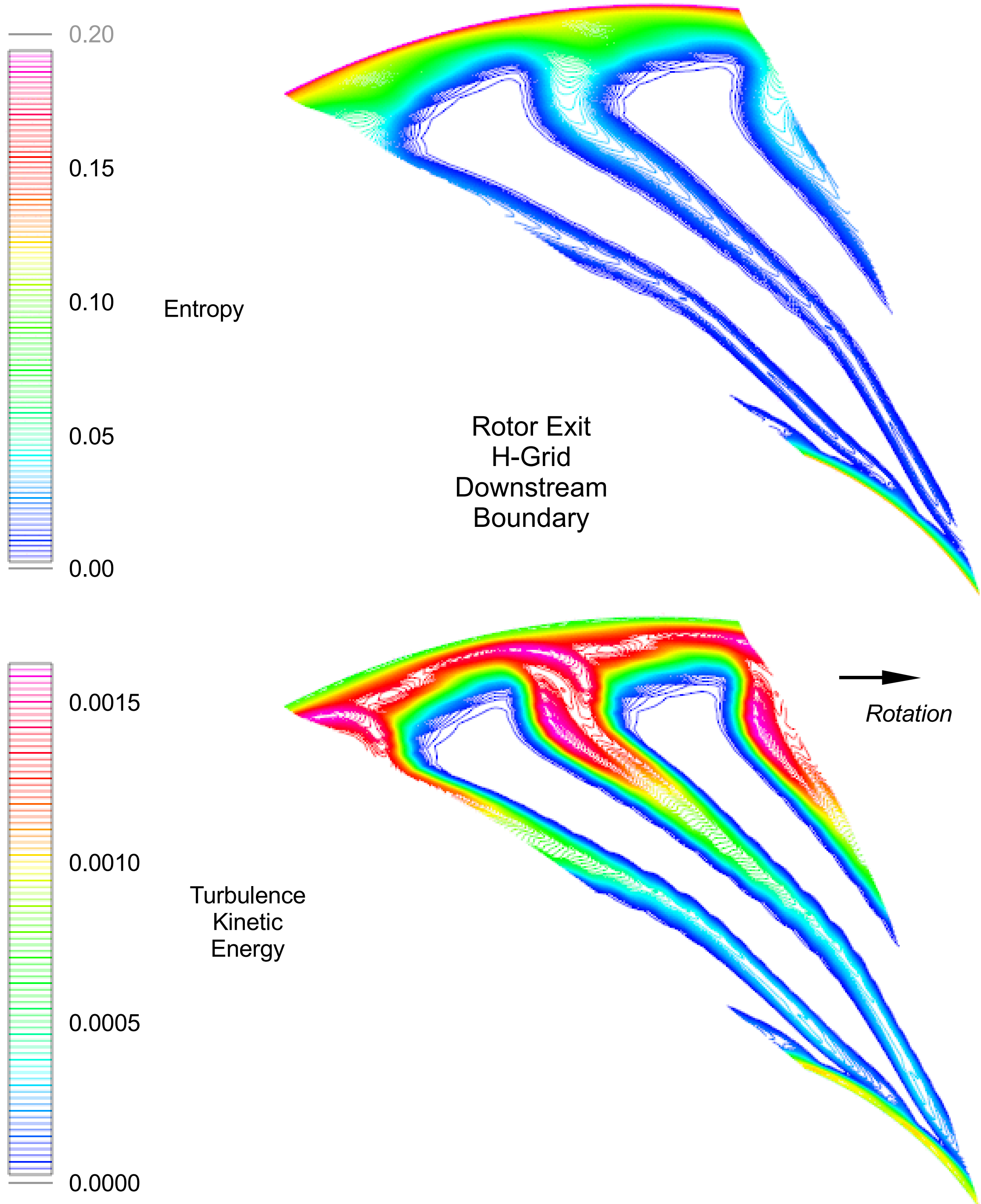

Figure 31b: Computed Rotor Flow Field for the Approach Operating Point; Downstream Mixing Plane; Entropy and Turbulence Kinetic Energy Contours

Approach Operating Point

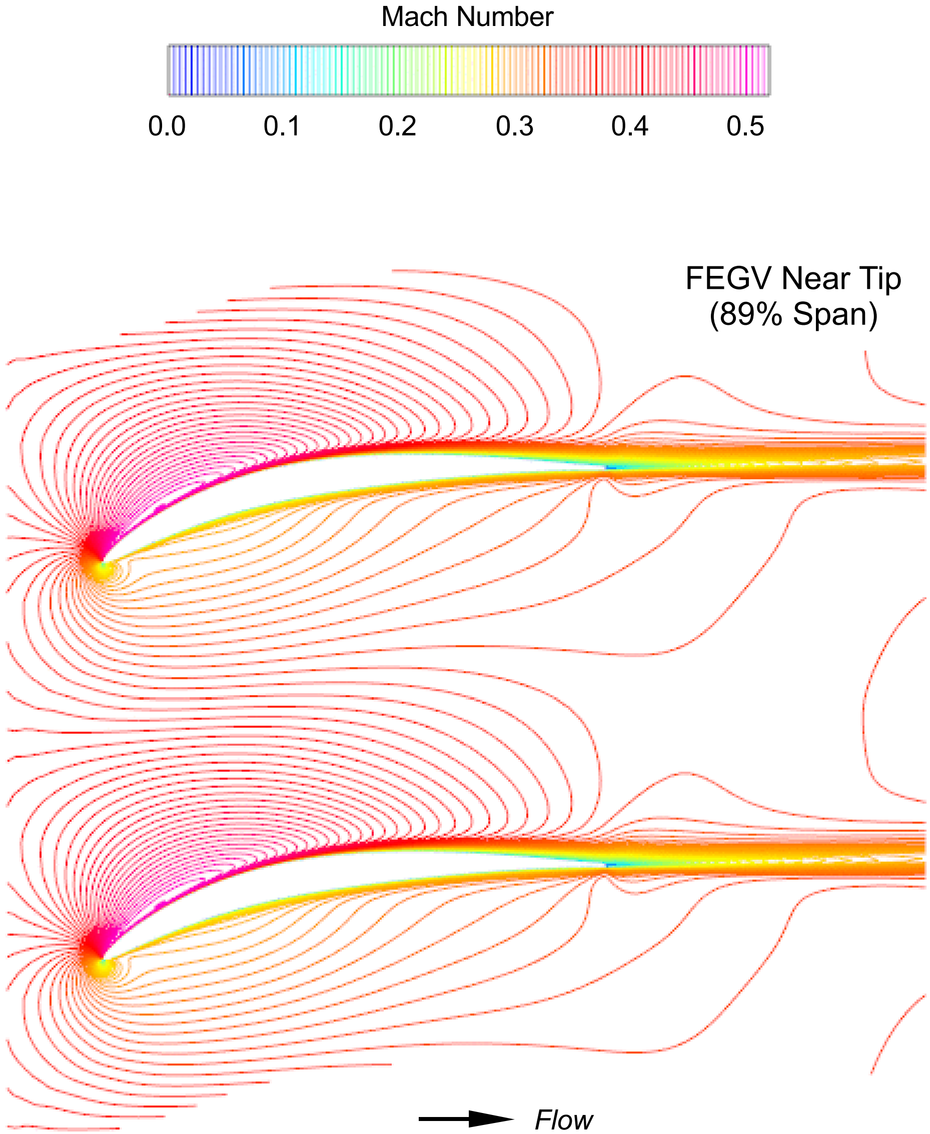

Figure 32a: Computed FEGV Flow Field for the Approach Operating Point; Blade-to-Blade Mach Number Contours

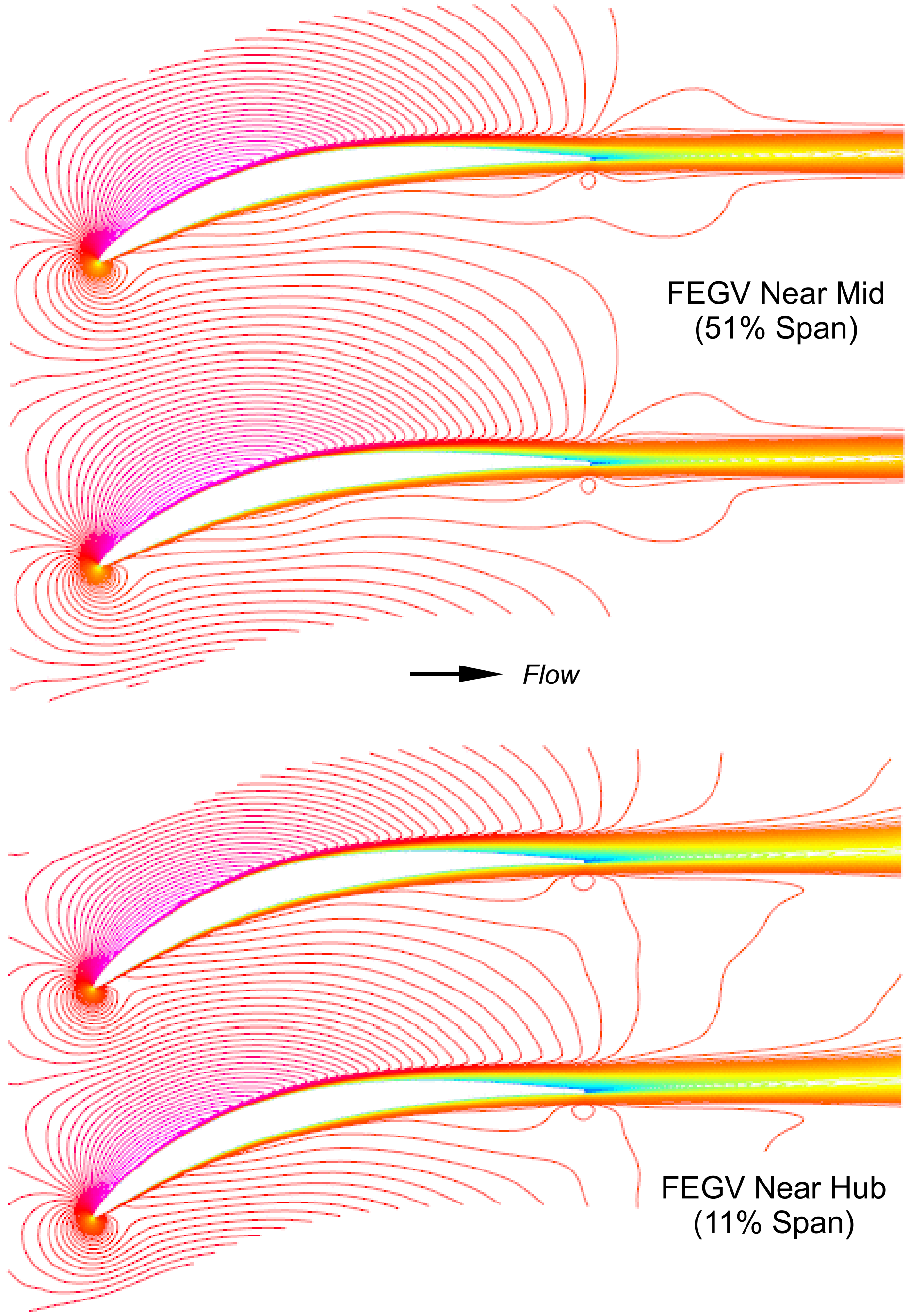

Figure 32b: Computed FEGV Flow Field for the Approach Operating Point; Blade-to-Blade Mach Number Contours

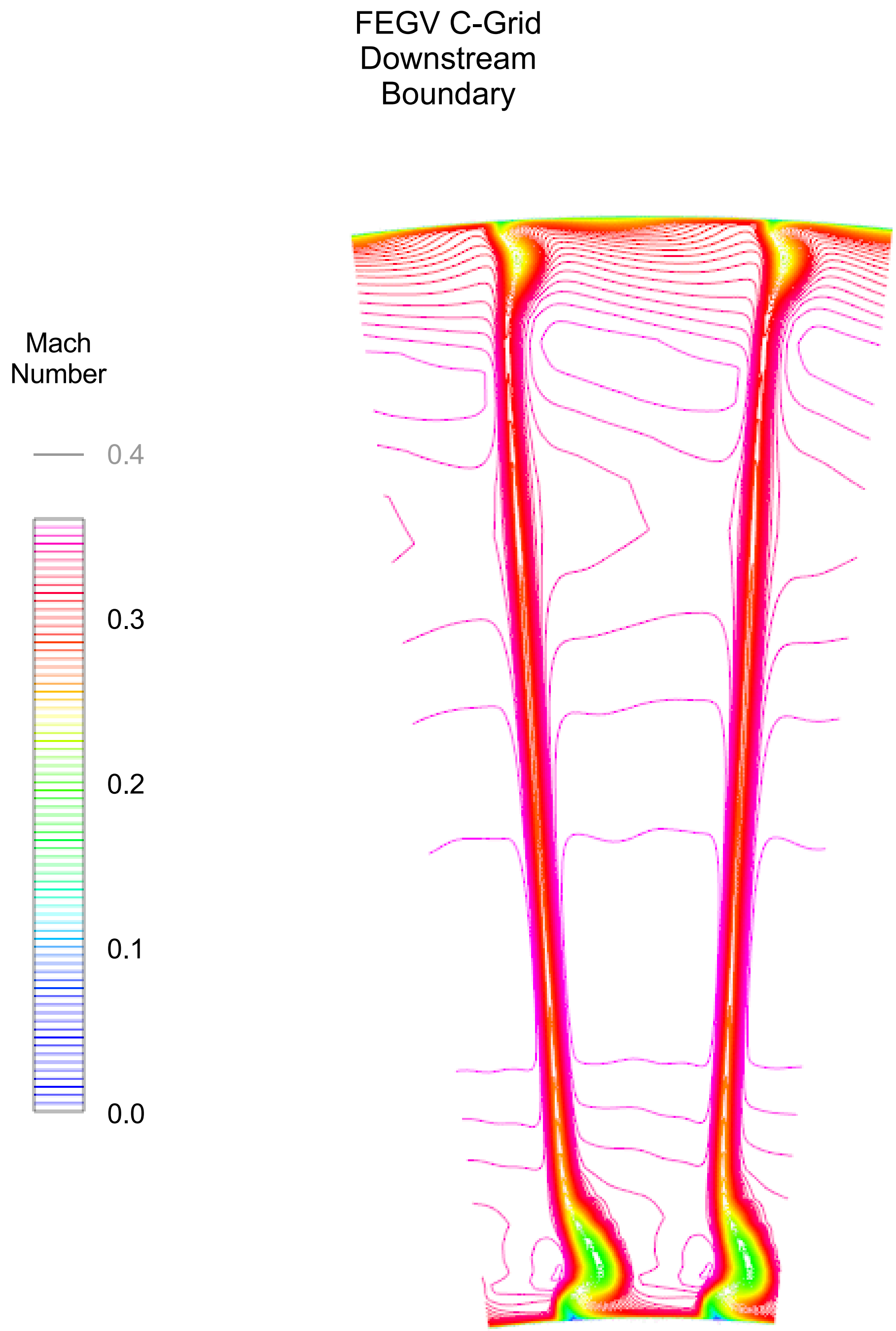

Figure 33: Computed FEGV Flow Field for the Approach Operating Point; Downstream Mixing Plane; Mach Number Contours

REPORT DOCUMENTATION PAGE						*Form Approved* *OMB No. 0704-0188*

1. REPORT DATE *(DD-MM-YYYY)*
01-10-2014

2. REPORT TYPE
Final Contractor Report

3. DATES COVERED *(From - To)*

4. TITLE AND SUBTITLE
Computational Aerodynamic Simulations of a 1215 ft/sec Tip Speed Transonic Fan System Model for Acoustic Methods Assessment and Development

5a. CONTRACT NUMBER
NNC06BA07B

5b. GRANT NUMBER

5c. PROGRAM ELEMENT NUMBER

6. AUTHOR(S)
Tweedt, Daniel, L.

5d. PROJECT NUMBER

5e. TASK NUMBER
NNC07E190T

5f. WORK UNIT NUMBER
WBS 473452.02.03.07.06.01.06

7. PERFORMING ORGANIZATION NAME(S) AND ADDRESS(ES)
AP Solutions, Inc.

8. PERFORMING ORGANIZATION REPORT NUMBER
E-18898

9. SPONSORING/MONITORING AGENCY NAME(S) AND ADDRESS(ES)
National Aeronautics and Space Administration
Washington, DC 20546-0001

10. SPONSORING/MONITOR'S ACRONYM(S)
NASA

11. SPONSORING/MONITORING REPORT NUMBER
NASA/CR-2014-218130

12. DISTRIBUTION/AVAILABILITY STATEMENT
Unclassified-Unlimited
Subject Category: 71
Available electronically at http://www.sti.nasa.gov
This publication is available from the NASA Center for AeroSpace Information, 443-757-5802

13. SUPPLEMENTARY NOTES

14. ABSTRACT
Computational Aerodynamic simulations of a 1215 ft/sec tip speed transonic fan system were performed at five different operating points on the fan operating line, in order to provide detailed internal flow field information for use with fan acoustic prediction methods presently being developed, assessed and validated. The fan system is a sub-scale, low-noise research fan/nacelle model that has undergone extensive experimental testing in the 9- by 15-foot Low Speed Wind Tunnel at the NASA Glenn Research Center. Details of the fan geometry, the computational fluid dynamics methods, the computational grids, and various computational parameters relevant to the numerical simulations are discussed. Flow field results for three of the five operating points simulated are presented in order to provide a representative look at the computed solutions. Each of the five fan aerodynamic simulations involved the entire fan system, which for this model did not include a split flow path with core and bypass ducts. As a result, it was only necessary to adjust fan rotational speed in order to set the fan operating point, leading to operating points that lie on a fan operating line and making mass flow rate a fully dependent parameter. The resulting mass flow rates are in good agreement with measurement values. Computed blade row flow fields at all fan operating points are, in general, aerodynamically healthy. Rotor blade and fan exit guide vane flow characteristics are good, including incidence and deviation angles, chordwise static pressure distributions, blade surface boundary layers, secondary flow structures, and blade wakes. Examination of the flow fields at all operating conditions reveals no excessive boundary layer separations or related secondary-flow problems.

15. SUBJECT TERMS
Low noise; Models; Scale models; Turbofans; Acoustic measurement; Aerodynamic

16. SECURITY CLASSIFICATION OF:			17. LIMITATION OF ABSTRACT	18. NUMBER OF PAGES	19a. NAME OF RESPONSIBLE PERSON
a. REPORT	b. ABSTRACT	c. THIS PAGE			STI Help Desk (email:help@sti.nasa.gov)
U	U	U	UU	54	19b. TELEPHONE NUMBER *(include area code)* 443-757-5802